

Dynamic Drop Models

P.M.C. de Oliveira¹, T.J.P. Penna¹, A.R. Lima²,
J.S. Sá Martins³, C. Moukarzel^{1,4} and C.A.F. Leite¹

¹ Instituto de Física, Universidade Federal Fluminense
av. Litorânea s/n, Boa Viagem, Niterói RJ, Brazil 24210-340

² P.M.M.H., École Supérieure de Physique et de Chimie Industrielles (ESPCI)
10, rue Vauquelin, 75231 Paris Cedex 05, France

³ Colorado Center for Chaos and Complexity, CIRES, and
Department of Physics, University of Colorado, Boulder, CO, USA, 80309.

⁴ Departamento de Física Aplicada, CINVESTAV Unidad Merida
Antigua carretera a Progreso, km. 6, 97310 Merida, Yuc., Mexico
e-mail: PMCO @ IF.UFF.BR

Abstract

We follow the dynamic evolution of a cluster of Ising spins pointing *up* surrounded by other spins pointing *down*, on a lattice. The cluster represents a liquid drop. Under a microscopic point of view, the short range ferromagnetic coupling between these spins plays the role of the van der Waals attraction. Alternatively, under a macroscopic point of view, the same ferromagnetic coupling gives rise to the surface tension along the drop boundary. This naive model is applied to the study of different systems, out of thermodynamic equilibrium. For each such a system, other interaction terms can be included, for instance an external magnetic field with a downwards uniform gradient, representing Earth's gravity. Also, for each system, proper dynamic rules and boundary conditions are adopted.

The behaviour of such a drop is monitored as a function of time, through computer simulations. Many quantities of interest, in particular those related to drop fragmentation, were measured and the results were compared with available experimental data. The real systems we have in mind are exemplified by water drops falling from a leaky faucet, nuclear multifragmentation, mercury drops falling on the ground, magnetic hysteresis curves, and interface roughness.

PACS: 75.40.Mg Numerical simulation studies

I – Introduction

The stationary geometry of a water drop pending from a vertical wall is an old mathematical puzzle (see [1] and references therein). A stochastic model [1] was applied as an alternative way to solve this puzzle. The drop is represented by a cluster of Ising spins pointing *up* ($S_i = +1$) on a square lattice (only the projection of the drop on the vertical plane perpendicular to the wall is of interest). All other lattice spins point *down* ($S_i = -1$), representing the air around the water drop. These spins are coupled through a first-and-second neighbour ferromagnetic interaction term strong enough to avoid the drop fragmentation. A non-uniform external magnetic field pointing also *up* is included, with the same intensity along each horizontal lattice row. However, this intensity increases uniformly when one goes from each row to the next one just below, i.e. there is a uniform vertical downward gradient which mimics the Earth's gravity. The Hamiltonian reads

$$\mathcal{H} = - \sum_{\langle ij \rangle} S_i S_j - g \sum_r r \sum_i S_i \quad , \quad (1)$$

where the first sum runs over all pairs $\langle ij \rangle$ of spins which are first or second neighbours on the square lattice. The index $r = 0, 1, 2 \dots$ counts the lattice rows downwards, and g is a free parameter representing the Earth's gravity intensity. The terms *up* and *down* refer to the Ising spin orientation only, they have nothing to do with the vertical axis of the square lattice where the drop is represented: they could be replaced by *wet* and *dry*, respectively.

The drop starts as half a circle glued on the upper part of the vertical wall represented by an external boundary lattice column, as schematically shown in figure I.1. Along this column, the upper spins point *up*, i.e. those in front of the drop diameter, while all other spins below it point *down*: the upper part of the wall is *wet*, in contact with the drop, but it remains *dry* below the drop. The spins along this boundary lattice column are kept **fixed** in this situation during all the drop time evolution. The ferromagnetic interaction term between the lattice spins and these fixed boundary spins keeps the drop glued on the wall and avoids it to slide downwards. A Monte Carlo updating of the spins outside this boundary wall is then performed in order to achieve equilibrium. Eventually, the geometrical aspect of the drop reaches statistical equilibrium; its **average** aspect can then be measured and compared with real drops [1]. Each updating step consists in choosing a random pair of spins, one pointing *up* along the drop's current inner boundary, the other pointing *down* along the current outer boundary. Then, both are flipped if this movement decreases the total energy given by equation (1) plus the wall boundary

condition. Accordingly, the drop mass (the total number of spins pointing *up*) remains unchanged, and only its geometrical shape is equilibrated by this relaxation process.

A very small artificial temperature could be included in order to decide to flip or not each previously tossed pair of spins. However, the only role played by this further artifact would be to avoid some possible trappings into metastable situations, during the evolution. According to our numerical experiments, the randomness in tossing the pair of spins to be flipped is enough to equilibrate the system, without need to resort to any further artificial thermal noise. Also according to our numerical experiments, one does not need to include second neighbour coupling into equation (1). The usual first-neighbour only interaction is enough. However, in this case, the geometrical shape of the drop is not so smooth, presenting mostly vertical or horizontal pieces along the surface: either a larger lattice or a larger number of averaging samples would be required in order to obtain the same accuracy.

The ferromagnetic coupling represented by the first summation of equation (1) obviously mimics an attraction between neighbouring water “molecules”, i.e. a “van der Waals term” keeping the drop connected into a single macroscopic piece. The same term can be rewritten as $2 \sum (1 - \delta_{S_i, S_j})$ plus an additive unimportant constant. Under this point of view, only the drop boundary contributes to the energy, i.e. it represents a surface tension which tends to minimize the drop perimeter. Indeed, only at the drop boundary one can find two neighbouring spins S_i and S_j , one pointing *up* inside the drop, the other *down* outside, contributing to the above sum. Otherwise, far from the boundary, one has $S_i = S_j$ (both neighbouring spins pointing *up* inside the drop, or both *down* outside), with no contribution to the above sum. Thus, the time evolution minimizing the energy given by the complete Hamiltonian (1) represents a competitive process between the first summation which tends to keep the drop spherical, and the second summation which tends to stretch it downwards. The Monte Carlo simulation performed in [1] studies the equilibrium compromise between these two opposed trends. In this case, the aim is simply to measure the geometrical shape of the drop at equilibrium, after performing some transient relaxation movements. Indeed, the geometry obtained in this way compares very well with real drops [1].

The same model can also be applied to the study of other systems which are really out of equilibrium. This was done by the authors during the last 8 years [2-12]. In this case, the interest is not to measure the equilibrium properties, but to follow the dynamic evolution of the system during its path towards equilibrium. This is the case of multifragmentation in both nuclear matter (section III) and mercury drops falling on the ground (section IV). It is also the case of annealing multilayered interfaces where a moving domain wall replaces

the drop (section VI). Other systems are continuously fed from outside, and never reach equilibrium. Examples are water drops falling from a leaky faucet (section II) or magnetic hysteresis loops (section V). In all cases, the same basic lattice drop model described above is adopted, with the surface tension term. In each case, some further ingredients are included into this basic model, according to the particular features of the system under study. The present text is a review of these works.

II – Leaky Faucets

The sequence of drops falling from a leaky faucet is a nice example of complex, long-term memory dynamics working in a simple real system. It became a paradigm for such dynamics after the work of R. Shaw [13]. Since then, many experiments were performed [14-28], running from the very simple to the very sophisticated. A spring-mass like model, first proposed by Shaw [13, 18, 29, 30] and improved by Fuchikami, Kyono and Ishioka [31,32], also provide very interesting descriptions of the complexity observed during drop formation. Apart from the geometrical aspect of a single drop itself, for which there are very beautiful experiments and simulations (see [5,19,23,28,31,32] and references therein), another interesting object to study is the sequence of time intervals measured between successive drops. This time series displays the quoted long-term memory dynamics. Very long time series, with over a million successive drops, taken with extreme care are available [20,4,21,23-26]. In spite of the term *chaotic* in the title of the original study [13], nobody knows if this dynamics is really chaotic: according to the available data, it seems to be complex, not chaotic. In [4], for instance, long-term anticorrelations were measured with very good accuracy, displaying the value $\alpha = 0.00$ for the Hurst exponent (see below) for many distinct experimental conditions. The same value with the same accuracy was measured from computer simulations [4] also for many distinct simulated conditions. Anyway, a conclusive definition of the character (chaotic, regular or complex) of this dynamics can be obtained only by measuring its Lyapunov exponent λ (> 0 , < 0 or $= 0$, respectively). Currently available data give $\lambda \approx 0$.

In this section we review some results obtained with a lattice drop model [2-5] based on that proposed by Manna, Herrmann and Landau [1] presented in the introduction. The model is very simple compared to others designed to simulate the formation of a single drop. However, as we have shown during the last years [2-5] it is also able to reproduce dynamical and morphological aspects of real drops.

In the model, the faucet is represented by W elements of fluid fixed in the center of

the first, top lattice row from which the drop pends. The flux of water is simulated by introducing F elements directly **on the outer boundary** of the drop at fixed intervals of time. Between successive injections of fluid, $N \times F$ relaxations are performed. This new parameter N is related with the viscosity of the fluid. The time can be defined as proportional to the number of relaxations performed since the beginning of the simulation. The disconnection of the drop is verified after each relaxation, and if it occurs, the disconnected piece is removed. The remaining fluid still pending from the faucet sets the initial condition for the next drop: it is responsible for the long-term memory.

The first question one can formulate about this model is if it could describe the morphology of real drops [5]. In order to answer this question we can follow some quantities like the volume, perimeter and center of mass height (measured downwards from the faucet) to compare with data available from real drops [23]. In figure II.1 we show some steps of the drop formation for $W = 40$, $N = 150$, $g = 0.1$ and $F = 20$. The numbers in the figure are the times when each image was obtained, counted since the last drop disconnection. We did not perform any averaging process to smooth the boundary.

In figures II.2, 3 and 4 we present the center of mass height *versus* time, area *versus* perimeter and perimeter/area *versus* time for the same drop in figure II.1. These results are essentially equivalent to that obtained from real drops [23]. Some features, like the formation of the “neck” before the complete disconnection of the drop, are present. A feature which is not present in the simulational results are the oscillations of the drop [23,31,32]. This is expected once the model does not consider inertia.

Our results show that the morphology of real drops can be reproduced by this simple model. We now turn our attention to a dynamics characterisation, through the analysis of the sequences of time intervals measured between successive drops, both in simulations and the experiment. This was first done by de Oliveira and Penna [2,3] and using more sophisticated techniques in [4]. Let’s call $\{B(n)\}$ the series of time intervals between successive drops. The main tool used to study such series is the reconstruction of the attractor of the system using return maps. The first return map, for instance, is obtained by plotting $B(n + 1)$ *versus* $B(n)$. In figure II.5 we show some first return maps constructed from time series obtained with the lattice model described in this chapter. These attractors and many others reproduce very well the real ones, mainly that produced by tiny faucets [17]. Different attractors are obtained varying the flux, just as in the experimental procedure.

The time series measured from successive drops falling from leaky faucets, experimental and simulated, are very similar [4] to the ones obtained from healthy heart beat intervals [33]. The authors of these references used the mean fluctuation in order to analyze the time series. This quantity is defined as (see, for instance [34])

$$F(n) = \langle |B(n' + n) - B(n')| \rangle_{n'} \quad , \quad (2)$$

where the brackets correspond to the average over all n' values. It measures the correlations at each time scale n , and behaves like

$$F(n) \sim n^\alpha \quad , \quad (3)$$

in the long-term limit $n \rightarrow \infty$. For healthy heart beat series the Hurst exponent is $\alpha \cong 0$. This means that the time series are in the extreme case of anticorrelation. For a random walk, the Hurst exponent is exactly $\alpha = 1/2$ (no long-range correlations at all), whereas $\alpha = 1$ for completely correlated systems. Actually, if the elements $B(n)$ of the time series are randomly shuffled, the exponent changes to $\alpha = 1/2$, which shows that we are dealing with a phenomenon dictated by the **chronology** according to which the successive heart beats occur. As obtained in [4], for both experimental and simulated time series, exactly the same thing occurs for the drops falling from leaky faucets. As examples of such measurements, in figure II.6 we show the fluctuation function calculated from the same simulated time series as presented in figure II.5. It is clear that for all the fluxes the Hurst exponent is equal to zero. Actually, the authors found $\alpha = 0.00$ [4] for all tested cases, within much larger time series, both experimental and simulated, with at least 10-fold larger accuracy than for the case of heart beats [33,34].

Another property which is the same for the time series of drops and heart beats is the probability distribution of the intervals $B(n)$ themselves. For both systems, it was shown [33-4] that it is well described by a Lévy distribution

$$P(I) = (1/\pi) \int_0^\infty \exp(\gamma q^\psi) \cos(qI) dq \quad , \quad (4)$$

where $I = B - \langle B \rangle_n$. For both systems one gets $\psi \cong 1.7$ ($\psi = 2$ would correspond to a Gaussian). The exponent $\psi < 2$ gives rise to a fat tail on the distribution plot, according to a power-law instead of the normal Gaussian exponential tail. The unimportant coefficient γ simply defines the distribution width. Note that α and ψ are independent exponents: α describes the particular chronology of events (it changes to $\alpha = 1/2$ under data shuffling), whereas ψ describes their intensities (does not change under shuffling). All these properties were obtained for different experimental and simulational conditions. Further comparisons of the leaky faucet and heart beat series were made by using other quantities, e.g. entropies and higher dimensional return maps [5]. The results suggested that a common physical mechanism, leading to long-term anticorrelations, could be present in both systems.

As mentioned in the beginning of this section, nobody knows if the leaky faucet is really chaotic. Up to now, different calculations have shown that the Lyapunov exponent could also be zero, but the precision is still unsatisfactory. This region is particularly difficult to study since the majority of methods available for Lyapunov exponent calculation assume exponential separation of orbits. However, the separation is not exponential if $\lambda = 0$. The suggestion that the Lyapunov exponent could be zero is mainly based on the fact that both leaky faucets and healthy hearts present long-term memory features, while any non-vanishing Lyapunov exponent $\lambda \neq 0$ would set a characteristic **finite** transient time $1/|\lambda|$ for the underlying dynamics. Moreover, as usual for biological systems, a healthy heart could follow a critical dynamic in the “edge of chaos” [33,34,11], i.e. with Lyapunov exponent $\lambda = 0$ for which the transient time diverges to **infinity**. This feature gives advantages in the adaptation of the system to unknown environmental changes [33-35]. The lattice drop model described here can be very useful to understand such properties. It allows one to generate very large time series in a fast and controllable way.

III – Nuclear Multifragmentation

The last two decades have seen an increasing interest in the experimental and theoretical study of heavy ions in collision. A major reason for this outburst is the expectation that at high enough energies, of the order of 200 MeV per nucleon, this system could probe the region in phase space where a transition liquid-gas has been predicted by a number of models for infinite nuclear matter [36]. In fact, the observed distribution of mass (or charge) of the intermediate mass fragments (IMF) generated by this process shows scale invariance along several decades; it has been claimed that the ubiquitous presence of this power-law for a number of systems of different compositions is a remnant, as observed in a finite system, of the above-mentioned transition. It has become standard practice in the literature to call nuclear multifragmentation the physical process that underlies these fractal and correlated distributions of IMF. Multifragmentation is then understood as the nuclear matter analog for the critical opalescence phenomenon observed in normal fluids.

As a theoretical support for this claim, the archetypical continuous transition in a percolation model has been examined. It could be shown, from simulational work, that the scale invariance for the distribution of cluster sizes present in the thermodynamical limit has a counterpart in finite, and small, systems [37]. Moreover, the correlations between the moments of various orders of this distribution, also present in this limit, still survive in the latter systems. Analysis of nuclear collision experiments, made on an

event-by-event basis, have shown a striking parallel with these numerical results on the percolation of small-sized systems. In particular, the critical exponents associated with the percolating transition, as revealed in small systems, appear to be, within errors, also valid for nuclear multifragmentation. Other than the exponent τ associated to the scale invariant distribution of IMF, defined through the equation

$$n(s, T) \sim s^{-\tau} f(T) \quad , \quad (5)$$

it has been claimed that the exponent γ according to which the susceptibility diverges in the infinite systems, defined through

$$M_2(T) \sim (T - T_c)^{-\gamma} \quad , \quad (6)$$

could also be determined from the experimental data, and that its value is again consistent with the percolation transition [38]. In the above equations, $n(s, T)$ is the distribution of IMF as a function of size s , $M_2(T)$ is the second moment of this distribution

$$M_k(T) = \sum_s s^k n(s, T) \quad , \quad (7)$$

T is the temperature of the system and T_c its critical value.

These results seem to support the analogy between percolation and nuclear multifragmentation, but are somewhat puzzling. Percolation is a geometrical and equilibrium continuous transition; on the other hand, it is not at all clear, and perhaps even not true at all, that the multifragmenting nuclei can be treated as an equilibrium system. One must add that a continuous transition needs fine tuning of at least one relevant scaling field, and multifragmentation appears to be present in a large range of different beam energies. In fact, the liquid-gas transition to which multifragmentation is referred is continuous only in a subspace of zero measure of phase space. These comments should suffice to justify an alternative approach to the problem that takes into account its intrinsic dynamical nature and that makes no *a priori* assumption on the order of the transition.

Dynamical models have been used recently to address multifragmentation, with some success; we mention here those based on quantum molecular dynamics [39], on cellular automata inspired by these dynamics [40], and on the lattice gas model [41]. Our approach to the problem bears some formal resemblance to the latter two; we model the compound intermediate nucleus at the freeze-out density as a lattice drop, a compact 3-D cluster of Ising spins pointing *up*, representing the nucleons, surrounded by spins pointing *down*, as mentioned in the introduction. The basic assumptions of the model can be summarized as:

- The entrance and exit channels are decoupled;
- The fragments come from the decay of a thermodynamically equilibrated, but still excited, source;
- Decay proceeds through surface rearrangements of the nucleons that compose the source, and through bulk radiative processes. Multifragmentation is the outcome of surface relaxation.

The dynamical evolution of the system starts at some chosen initial temperature, related to the excitation energy of the system. The subsequent motion in phase space follows the general rules stated in the introduction, with an Ising Hamiltonian that includes coupling with nearest and next-nearest neighbours (hereafter, $g = 0$). In this case, the flipping of spins is accepted through a Metropolis algorithm. The result of these update rules is a Kawasaki-like dynamics, with conservation of “magnetisation,” or mass (number of nucleons), which causes a continuous reshaping of the surface of the system. One can associate this dynamics to a canonical walk on the landscape generated by the surface part of the system’s free energy. After each successful flipping, the (surface) energy variation that it entails is recorded and the resulting drop geometry is examined for compactness. If it has become two disjoint blobs, the smallest one is called a fragment, its mass included in a statistical distribution, and it is erased from the rest of the simulation; the accumulated variation in the system’s energy since the last fragment was formed is then taken into account, resulting in a new value for the excitation energy of the nucleus. Other than this surface relaxation process, a bulk radiative decay is also simulated. After each fixed number of Monte Carlo time steps, the excitation energy is decreased by a constant factor, generating an exponential decay. The combination of these two parameters represent in fact a ratio between the intensity of surface and bulk processes, and play an interesting role in what follows. A complete description of the model can be found in [8], together with comments on its computer implementation.

An important final detail relates to the way in which the running value of the excitation energy generates a thermodynamic temperature for the system. This relation is usually called the caloric curve in the nuclear physics community, and its actual shape or analytical expression has been the subject of intense study and controversy in recent years. In our simulations, we used two different forms for this caloric relation, a Boltzmann gas-like linear relation $T \sim E$ and a quadratic Fermi gas-like $T \sim \sqrt{E}$.

We present in figure III.1 the correlations between moments of higher orders of the fragment distribution seen both in the experiments and in our simulations. For a distribution satisfying a static scaling *ansatz* these correlations can be derived analytically and read in general

$$\log(M_k(T)) \sim \lambda_{k/j} \log(M_j(T)) \quad . \quad (8)$$

The slope $\lambda_{k/j}$ of these $\log \times \log$ plots can be related to the Fisher exponent τ , and have to satisfy a consistency equation near criticality, as shown in [37]:

$$\tau = (j + 1) - (k - j)/(\lambda_{k/j} - 1), \quad (k' - j)\lambda_{k/j} - (k - j)\lambda_{k'/j} = k' - k \quad . \quad (9)$$

The consistency equation can be used in the simulations to identify the realisations that most closely follow the correlations expected in the thermodynamical limit, and from these one can infer the value for τ . Proceeding in this manner, we found $\tau = 2.18$, the same for both caloric curves and in accordance with the value inferred from the experiments.

For the determination of a second critical exponent we followed guidelines put forth in [38] when dealing with the same problem for the experimental data. The central idea is to explore the equality of the exponent γ for the second moment of the distribution when calculated above and below the transition. As an interesting by-product, this technique enables a more precise determination of the transition point. One proceeds in analogy with percolation in finite lattices, where the order parameter is the density of the percolating, or largest, cluster. This cluster is not considered for the second moment of the distribution in the liquid phase, or below the transition, where it is the seed for the nucleation of the stable phase. For the gas phase, above the transition, all clusters are considered. By a trial and error procedure, these moments are calculated for each candidate to the transition point in a certain range, and the slopes of a $\log \times \log$ plot as a function of the parameter measuring the distance to the transition point are compared. A best match between the two is the criterion that determines the critical point, and γ is also immediately available. Figure III.2 illustrates the procedure and shows the best determination for both the transition point and the exponent γ for a Fermi-gas caloric curve and a particular value for the surface-to-bulk time scale ratio $a = 0.998$. The value found, $\gamma = 1.80$, is again consistent with the conjecture that puts nuclear multifragmentation in the universality class of $3D$ percolation. Contrary to the robust value of $\tau = 2.18$, it was also found that these last choices ($T \sim \sqrt{E}$ and $a = 0.998$) have a definite impact on the exponent γ . Although also found in solvable models such as the eight vertices model [42], where it can be related to a marginal scaling field, this rather unusual continuous dependence of a critical exponent on a parameter is worth mentioning. In particular, a conjecture [43], relating the controversy among experimental groups about the value of γ to the particular pair target-beam used and the resulting differences in surface-to-bulk relaxation time scales, appeared in the literature shortly after our result was first published [9].

To summarize, we have shown that simulations of a lattice model, evolving through dissipative surface and bulk relaxation, with Metropolis dynamical rules and a short-range Ising Hamiltonian, can reproduce both qualitative and quantitative aspects observed in nuclear multifragmentation. This agreement supports the claim that the relevant physics of the processes involved does not depend on the microscopics of the interactions, which would be in any case unlikely to be derived from first principles, and to which one has only indirect access, if any. It is not incidental that a pathway like ours can suggest and support new relevant physics, such as pointed out in the last paragraph: by focusing on a few well chosen features of the phenomena being studied, the role of each can be more adequately explored. This newly acquired knowledge will in turn support the choices to be made in the next generation of models, in a fast growing evolutionary chain made possible by the simulational approach.

IV – Mercury Drops

A nice experiment was introduced in [44]. A mercury drop falls from a certain height on the floor. As a consequence of the collision, fragments are formed. By classifying these fragments by size (or mass) according to a logarithmic scale (bins), and counting how many of them exist within each class, one can measure the size distribution probability. Good statistics would be achieved after many repetitions of the experiment, starting with the same initial drop as well as the same falling height, superimposing all countings at the end. This process is similar to the nuclear multifragmentation experiment described in the previous section. One can also predict a similar behaviour: a broad distribution of fragment sizes could appear, perhaps following some power-law.

The outcome of the experiment [44] is not a simple power-law. By plotting the countings according to a $\log \times \log$ scale, one has indeed a broad distribution of fragment sizes, but not a single straight line. Instead, the experimental data is better fitted by two straight lines (see figure IV.1, to be described later). A crossover point in between the small- and large-fragment regimes appears as a rounded knee on this experimental plot. The drop-counting strategy adopted by the authors of [44] is a hard one: each fragment is measured through a microscope. That is why their experimental data do not present a very good statistics, and a precise definition of the mathematical form of the distribution cannot be inferred, moreover for the small-drop limit. Contrary to figure IV.1, the left part of the corresponding plot presented in [44] seems to approach a horizontal line, indicating some sort of counting saturation for smaller and smaller fragments. We credit this feature to

an underestimated counting of small fragments at the microscope, not to a real saturation effect.

That is why we decided to repeat the experiment following an alternative strategy: we take a photograph of the fragments, which is then digitalised by using a scanner. The fragment counting was then performed by a computer program. This procedure gives us confidence in the small-drop counting, as compared with [44]. Our first, preliminary results show the same behaviour as in [44] for large fragments, and are displayed in figure IV.1. It corresponds to two different falling heights $h = 220$ cm and 240 cm, with 10 realisations of the experiment for each height. Once we used real photographic paper, with a much higher resolution than the scanner, our experiment is limited only by the latter. Thus, it is possible to improve our results by including smaller yet drops into the statistics (figure IV.1 was prepared with a low scanner resolution, due to limitations of memory and time on our outdated computer). For the present work, nevertheless, the preliminary results of figure IV.1, already with a much better counting of small fragments as compared with [44], are enough in order to test our dynamic lattice drop model as applied to this problem. Experimental improvements are in course and will be presented elsewhere.

Let's describe now our dynamic model. The computer simulations starts at the very moment when the initial mercury drop reaches the floor. It is represented by a round cluster of N black pixels (spins *up*) on a square or cubic lattice, just touching the floor represented by an inert bottom boundary. The total kinetic energy E , proportional to the falling height already traced downwards, is given since the beginning. Being a coherent kinetic energy before the crash, it is shared among all drop pixels, each one carrying an amount of $e = E/N$. The temperature is set to $T = 0$, once one has no random motion yet. From this initial situation, the collision with the floor will be performed as follows, step by step: *i*) the n pixels currently touching the floor are transferred to random positions at the current free surface, and the drop as a whole is moved one row down; *ii*) the energy e carried by each one of these n pixels is set to 0, decreasing the coherent kinetic energy of the whole drop; *iii*) the same decrement ΔE is transformed in incoherent, thermal energy, by increasing the temperature from T to $T + \Delta E$; *iv*) The drop shape is then allowed to relax, by performing r movements exchanging the positions of a spin *up* with another spin *down*, both randomly chosen at the current free surface, according to the Metropolis rule under temperature T for the first-and-second neighbour Ising Hamiltonian. This last step is the same already used before for the leaky faucet and nuclear multifragmentation. The four steps are repeated iteratively.

At some moment during this process, some piece of the drop becomes disconnected from the main part still touching the floor. This piece is considered a fragment. If,

due to this fragmentation, the energy of the whole system increases, then this fragment is discarded and counted into the statistics. Also in this case, the temperature T is decreased to $T - kE_f$, where E_f is the surface energy carried out by the fragment. The dynamics described in the last paragraph goes on, further relaxing the remainder drop. The process stops when the drop vanishes, or when the temperature is low enough to avoid any further activity. The whole process is performed again and again, starting always from the same initial drop with the same initial energy, in order to accumulate a good statistics. At the end, the fragments are classified by their sizes (mass), according to a logarithmic scale (bins), taking into account all realisations performed with the same initial energy.

Figures IV.2 and 3 show two typical distributions obtained by our model, to be compared with the experimental counterparts in figure IV.1. The general behaviour with two power-law regimes, one for small and the other for large fragments, is obtained always for a lot of different choices for the set of parameters E , r and k , both for the square and the cubic lattice. Note that our simulational statistics is much higher than the experimental one. In spite of the striking similarity between these simulational results and the experimental observations, at the present moment we consider our model still very crude in order to allow any quantitative comparison. Both our experiments and simulations are still in a preliminary stage. Anyway, looking to Figures IV.1, 2 and 3, we can hope our naive model could be useful in understanding the addressed physical problem. At least two points are still missing: *i*) a better definition of the experimental curve, figure IV.1, by improving both the resolution as well as the statistics; *ii*) a theoretical explanation for the crossover between the small and large fragment regimes, which is already evident in both our experiment and simulation.

V – Magnetic Hysteresis

A nice example of non-equilibrium physical behaviour is the hysteresis curve, magnetisation *versus* applied magnetic field. Consider a virgin sample of some ferromagnetic material below its Curie critical temperature. Virgin means that the sample is not magnetised yet, i.e. it was never exposed to any external magnetic field. One can obtain such a sample simply by heating it far above the Curie temperature, and then allowing it to return back to a lower temperature, free from any external magnetic field. In this case, inside each magnetic grain of the sample one can find different magnetic domains, separated from each other by domain walls. As the magnetic axis inside each domain points in a random direction, the whole grain (and thus also the whole sample) presents a

macroscopically vanishing magnetisation.

Consider now the sample kept under a fixed temperature, below the Curie point. Applying a small external magnetic field, some few domains already parallel to the field are enlarged, at the expenses of other neighbouring domains which shrink. As a result, the sample presents now a small macroscopic magnetisation, far below its maximum possible saturation value. This occurs because other domains, for which the external field is not strong enough to provide the energy necessary to jump the barrier corresponding to flipping the spins near the domain wall, remain as they were before the external field was applied. By increasing a little bit the external field, the whole magnetisation is supposed also to increase proportionally to the (still small) field. Thus, the plot magnetisation *versus* field follows more or less a straight line, starting from the origin (see the beginning of the curve in figure V.7, just below the symbol 0, to be explained later).

However, this linear dependence between magnetisation and external field cannot continue for larger values of the field. Experimentally, as the external field is gradually increased, one observes first a change in the slope, the magnetisation increasing faster and faster in response to the applied field. Later, for high enough values of the external field, the magnetisation eventually saturates, all magnetic domains of the sample pointing in the same imposed direction (see branch 0 of figure V.7).

The explanation for this behaviour is simple. Some domain walls, particularly where impurities are absent, can easily be deformed just by transferring a spin from one magnetic domain to another neighbouring one (i.e. a domain wall movement). A simple example is shown in figure V.1, where a 64×32 “grain” of Ising spins displays two magnetic domains. No external field is yet applied, and the magnetisation still vanishes. Spins near the domain wall are easier to be flipped than other spins deep inside each domain. Along the wall, however, spins near the grain boundary, i.e. those touching the upper or the lower row in figure V.1, are not so easy to be flipped, because they are pinned by the non-magnetic material outside the grain. Thus, by applying a small magnetic external field, the result is a round domain wall, as shown in figures V.2 and V.3, instead of the flat one in figure V.1. The magnetisation increases, in response to the applied field, but not so much.

Within our simple model, in order to mimic this pinning effect, we adopted the following boundary conditions for spins at the upper or lower rows. For these sites, instead of 8 neighbouring spins (first and second neighbours on the square lattice), one has only 5. The 3 missing neighbours are then supposed to point in the same direction of the spin currently being updated. Now, instead of choosing a pair of spins, one *up* and the other *down*, one chooses only a random one, *up* or *down*, along the domain wall. It will be flipped or not, according to the canonical Boltzmann weight $\exp(-\Delta E/T)$, where ΔE is

the energy increment due to flipping. In order to compute this energy jump ΔE , besides the external field, one takes into account the Ising coupling energy between the tossed spin and its 8 fixed neighbours. Would this spin be tossed at the grain boundaries, the 3 missing neighbours (supposed to be parallel to it) would give always a positive contribution to ΔE , thus difficulting the flipping as compared to other spins along the domain wall. Figures V.1 ... 6 show snapshots of the Ising spins on our 64×32 grain, for increasing values of the external magnetic field h . The magnetisation m increases slowly for figures V.1, 2 and 3, for which the domain wall remains pinned at the grain boundaries: it is bent but does not slide yet. In figure V.4, however, the external field is already strong enough to force the domain wall to slide against the boundary pinning: the magnetisation starts to increase according to a larger rate, as in figure V.5. Finally, figure V.6 shows the situation where the magnetisation is already saturated. The complete plot magnetisation *versus* field corresponds to the branch denoted by 0 in figure V.7. The field is gradually increased, in steps of $\Delta h = 0.01$. In between two successive field upgrades, $M = 100$ spin flips are tried along the current domain wall.

The branch denoted by 1 in figure V.7 corresponds to decreasing the field back, following the same steps. Only for already negative values of the field, the magnetisation starts to decrease again from its saturation value. Eventually, after crossing the value 0 at the so-called coercitive field, it becomes again parallel to the external field, and saturates for large enough negative values of the field. The last branch denoted by 2 in figure V.7 corresponds to another field sweep, again step by step, now from negative to positive values. One can obtain different hysteresis curves like that, by changing the values of M and/or Δh , as well as the fixed temperature T adopted in order to decide to flip or not the tossed spin.

VI – Annealing Effects in Multilayers

Using the ideas introduced in the previous sections, the same model was adopted [12] to study the annealing effects on multilayers. Such study was motivated by the experimental fact that electronic properties of multilayered systems can be strongly affected by the quality of their interfaces. A couple of examples are the giant magnetoresistance effect (GMR) and the interlayer magnetic coupling [45-47]. Therefore, the control of interfacial roughness and interdiffusion is an important issue both for basic research and for the use of those systems in electronic devices.

In that study [12], a two-dimensional system made of immiscible materials A and B

was considered, consisting of a stripe of material A sandwiched by B. L and H represent the lateral dimension and height of the whole system, respectively, and W is the mean width of stripe A (see figure VI.1). An example of real system composed by two immiscible materials arranged in such a way are Co/Ag multilayers (see [48] and references therein). For this system it was suggested that the interfacial roughness displays a minimum as a function of the annealing temperature. It has also been found that relatively thin Co layers may break, forming clusters, for sufficiently high annealing temperatures [48].

Each spin S_i of our model takes the values ± 1 , depending on whether the site i is occupied by an A (+1) or B (-1) atom. The Ising energy summation runs **over pairs of nearest neighbours only** and the interaction favours agglomeration of atoms of the same type. Now, the role of temperature is crucial. The system is placed in contact with a heat bath at a temperature T , and a spin-flip (AB interchange) Monte Carlo dynamics is performed by Kawasaki trials, where pair updates are made, conserving both the numbers of A and B atoms [49]. This is executed by randomly choosing one site A at the interface, and interchanging it with a **nearest neighbour B atom, also picked at random**. Such interchange preserves the total number of atoms of each species, but may change the total energy of the system by ΔE . The Metropolis algorithm is then used to define the acceptable interchange trials, according to the ratio $\Delta E/T$, where the Boltzmann's constant is set to unity. The first and last rows are fixed with W adjacent A atoms each, face to face, in order to avoid lateral motion of the stripe of A atoms. This could be interpreted as a surface effect.

The annealing process is simulated as follows: we take a system with randomized interfaces, in which layer A has mean width W with maximum mean square deviation δ . The system is then thermalized at a given temperature T_a , allowing for n_a interface relaxations. The temperature is gradually reduced, in steps dT , until it reaches a value T_0 . After each temperature reduction, n_T interface relaxations are performed. The parameter n_a regulates the amount of time the sample was kept at temperature T_a , and n_T controls the rate at which the temperature is reduced from T_a to T_0 . Roughness is measured by computing $\sigma = \sum_{\langle ij \rangle} (1 - S_i S_j) / 2 - 2H/a$, where a is the lattice constant. Clearly, for perfectly flat interfaces one has $\sigma = 0$, and it increases with A-B interdiffusion.

For this problem, the interest is to calculate the mean roughness variation $\langle (\sigma_f - \sigma_i) / \sigma_i \rangle$, as a function of the annealing temperature T_a , for several widths W . Here $\langle \dots \rangle$ represents an ensemble average over N samples, whereas σ_i and σ_f are the corresponding values of σ before and after the annealing process is executed. Some results are shown in figure VI.2. Lengths are measured in units of a . The calculations were made for $N = 100$ different samples, all with $H = 150$, $L = 40 + W$, and $\delta = 2$. We assume that T_a is reduced

down to $T_0 = 0.01$ in steps of $dT = 1/32$, with $n_a = 20$ and $n_T = 10$. It is evident from figure VI.2 that the mean roughness variation has a minimum, as experimentally inferred. Its position does not depend much on W , and we have also verified that for different values of H , L , n_a , n_T and δ (provided that $\delta \ll W$), the results follow the same behaviour, all showing a clear minimum at $T_a \cong 1.2$. The insets depict snapshots of the final interface configuration at T_0 for some values of T_a . It is clear that for certain values of W and high enough values of T_a , the A layer may break into clusters. This effect can also be studied by this kind of model.

It was also shown [12] that some quantities as the average number of A atoms having z first and second nearest neighbours of type B, for different values of T_a , provide results similar to the experimental ones obtained by nuclear magnetic resonance experiments [50]. Since this simple model is able to produce layers with controllable roughness (determined by the annealing temperature) it can be very useful to study transport properties on multilayers. Work along these lines is in progress.

VII – Conclusions

Critical equilibrium situations occur in many systems in Nature. Generally, by varying some external control parameter T (temperature, for instance) the system can suffer a continuous phase transition when some critical value T_c is surpassed. By keeping the system in equilibrium just at T_c , its behaviour becomes completely distinct from that observed both above and below T_c . Instead of the normal exponential decaying of spatial correlations (in general) observed by increasing the distance between two points randomly picked inside the systems, just at T_c these same correlations decay as power-laws. The exponential decaying feature provides a well-defined length scale $\xi(T)$ for the system at $T \neq T_c$: two different positions separated by a distance larger than $\xi(T)$ barely influence each other. One can consider the system as composed by finite pieces with typical length $\xi(T)$ each: the behaviour of the system as a whole is simply obtained by adding the extensive quantities (energy, mass, magnetisation, etc) corresponding to its component pieces treated separated from each other. The system is linear, in the sense that the whole is the sum of the parts.

On the other hand, just at T_c , the lack of an exponential decaying gives rise to an equivalent lack of any characteristic length scale: the system no longer behaves as the linear superposition of finite pieces, and all length scales must be taken into account. The adequate theory to treat such singular, critical equilibrium situations was awarded with

the 1982 Nobel prize for Kenneth Wilson (see [51] for a friendly introduction). According to it, instead of the linear behaviour, successively performed length scaling operations, i.e. successive zooms multiplying by λ the unit length of its component pieces, lead to successive multiplications of some quantity Q by λ^{ϕ_Q} , where the exponent ϕ_Q is characteristic of each quantity Q . Note that a power-law relation between Q and the length L is invariant under such an endless scaling procedure, but not an exponential decaying relation which would fast vanish, instead.

The distinguishing feature of critical situations is the universality: the same set of critical exponents ϕ_Q for the various quantities of interest holds for entire classes of different systems and models. Only some general characteristics of the system, namely its geometrical dimension and the symmetries of its order parameter suffice to define its critical equilibrium behaviour. For instance, in spite of the quantum character and the complicated interactions between neighbouring molecules, the critical behaviour of water at $T_c = 374^\circ\text{C}$ can be modeled by a simple three-dimensional Ising ferromagnet! This is only a striking example among a huge set of others where universality is observed. That is why models very simplified at the microscopic level can be applied with success to study the critical equilibrium behaviour of a much more complicated real system. These lines were extensively followed during the last four decades, within the fast growing research field of critical equilibrium phenomena.

Concerning non-equilibrium systems, too, examples of critical dynamics are numerous. In this case, a power-law decay behaviour in **time**, besides length, also appears. This means that the dynamic evolution of such systems is insensitive to **short-term** simplifications, besides the microscopic details above mentioned. A striking example of this robustness was shown in [27], where the leaky faucet experiment was performed with clusters of ants pending from a thin vertical rope, instead of water drops. The ants go by themselves to this rope, one after the other, forming a growing cluster. Suddenly, a drop of them falls, but some few ants still remain pending from the rope, giving rise to a new growing drop. The “short-range coupling” between ants glued on each other has nothing to do with the van der Waals attraction between water molecules, neither with the simplified coupling between neighbouring Ising spins. Nevertheless, exactly the same results described in section II were also obtained in [27], with ants. In the present work, we have exhibited some examples where a simple drop dynamic model reproduces very well the behaviour of real systems. The common feature among these otherwise completely distinct systems is the fact that they all present **long-term** memory features, allowing us to apply our very simplified model.

Acknowledgements

We are indebted to Jürgen Stilck and Dietrich Stauffer for critical readings of the manuscript. This work was partially supported by Brazilian agencies CAPES, CNPq and FAPERJ. J.S.S.M. is supported as a Visiting Fellow by CIRES, University of Colorado at Boulder.

References

- [1] S.S. Manna, H.J. Herrmann and D.P. Landau, *J. Stat. Phys.* **66**, 1155 (1992).
- [2] P.M.C. de Oliveira and T.J.P. Penna, *J. Stat. Phys.* **73**, 789 (1993).
- [3] P.M.C. de Oliveira and T.J.P. Penna, *Int. J. Mod. Phys.* **C5**, 997 (1994).
- [4] T.J.P. Penna, P.M.C. de Oliveira, J.C. Sartorelli, W.M. Gonçalves and R.D. Pinto, *Phys. Rev.* **E52**, R2168 (1995).
- [5] A.R. Lima, T.J.P. Penna and P.M.C. de Oliveira, *Int. J. Mod. Phys.* **C8**, 1073 (1997); A.R. Lima, *MSc. Thesis*, Universidade Federal Fluminense, Niterói, Brazil (1997).
- [6] P.M.C. de Oliveira, J.S.S. Martins and A.S. de Toledo, *Phys. Rev.* **C55**, 3174 (1997).
- [7] P.M.C. de Oliveira and A.P. Guimarães, *Monte Carlo Simulations of Hysteresis Loops*, International Conference on Magnetism (1997), Cairns, Australia (unpublished).
- [8] J.S.S. Martins and P.M.C. de Oliveira, *Int. J. Mod. Phys.* **C9**, 867 (1998).
- [9] J.S.S. Martins and P.M.C. de Oliveira, *Nucl. Phys.* **A643**, 433 (1998).
- [10] P.M.C. de Oliveira, J.S.S. Martins, C. Moukarzel and C.A.F. Leite, *Falling Mercury Drops*, Workshop on Complex Systems (1998), Brasília, Brazil (unpublished).
- [11] S. Moss de Oliveira, P.M.C. de Oliveira and D. Stauffer, *Evolution, Money, War and Computers: Non-Traditional Applications of Computational Statistical Physics*, section 3.3, B.G. Teubner, Stuttgart Leipzig, ISBN 3-519-00279-5 (1999).
- [12] A.R. Lima, M.S. Ferreira, J. d'Albuquerque e Castro and R.B. Muniz, to appear in *J. Magn. Magn. Mater.* (2000).
- [13] R. Shaw, *The Dripping Faucet as a Model Chaotic System*, Aerial Press, Santa Cruz, California (1984).
- [14] P. Martien, S.C. Pope, P.L. Scott and R. Shaw, *Phys. Lett.* **110A**, 339 (1985).
- [15] H.N.N. Yépes, A.L.S. Brito, C.A. Vargas and L.A. Vicente, *Eur. J. Phys.* **10**, 99 (1989).
- [16] X. Wu and A. Schelly, *Physica* **D40**, 433 (1989).

- [17] K. Dreyer and F.R. Hickey, *Am. J. Phys.* **59**, 619 (1991).
- [18] J. Austin, *Phys. Lett.* **115A**, 148 (1991).
- [19] X.D. Shi, M.P. Brenner, and S.R. Nagel, *Science* **265**, 219 (1994).
- [20] J.C. Sartorelli, W.M. Gonçalves and R.D. Pinto, *Phys. Rev.* **E49**, 3963 (1994).
- [21] R.D. Pinto, W.M. Gonçalves, J.C. Sartorelli and M.J. de Oliveira, *Phys. Rev.* **E52**, 6896 (1995).
- [22] G.I.S. Ortiz and A.L.S. Brito *Phys. Lett.* **203A**, 300 (1995).
- [23] M.S.F. da Rocha, J.C. Sartorelli, W.M. Gonçalves and R.D. Pinto, *Phys. Rev.* **E54**, 2378 (1996); M.S.F. da Rocha, *MSc. Thesis*, Universidade de São Paulo, São Paulo, Brazil (1996).
- [24] J.G. Marques da Silva, J.C. Sartorelli, W.M. Gonçalves and R.D. Pinto, *Phys. Lett.* **226A**, 269 (1997).
- [25] W.M. Gonçalves, R.D. Pinto, J.C. Sartorelli and M.J. de Oliveira, *Physica* **A257**, 385 (1998).
- [26] R.D. Pinto, W.M. Gonçalves, J.C. Sartorelli, I.L. Caldas and M.S. Baptista, *Phys. Rev.* **E58**, 4009 (1998).
- [27] E. Bonabeau, G. Theraulaz, J.-L. Deneubourg, A. Lioni, F. Libert, C. Sauwens and L. Passera, *Phys. Rev.* **E57**, 5904 (1998).
- [28] S.R. Nagel, *Am. J. Phys.* **67**, 17 (1999).
- [29] G.I. Sánchez-Ortiz and A. L. Salas-Brito, *Physica* **D89**, 151 (1995).
- [30] A. d’Innocenzo and L. Renna, *Phys. Lett.* **220A**, 75 (1996).
- [31] N. Fuchikami, S. Ishioka and K. Kiyono, *J. Phys. Soc. Jpn.* **68**, 1185 (1999).
- [32] K. Kiyono and N. Fuchikami, *J. Phys. Soc. Jpn.* **68**, 3259 (1999).
- [33] C.-K. Peng, J. Mietus, J.M. Hausdorff, S. Havlin, H.E. Stanley and A.L. Goldberger, *Phys. Rev. Lett.* **70**, 1343 (1993).
- [34] H.E. Stanley, S.V. Buldyrev, A.L. Goldeberger, Z.D. Goldberger, S. Havlin, R.N. Mategna, S.M. Ossadnik, C.-K. Peng and M. Simons, *Physica* **A205**, 214 (1994).
- [35] P.M.C. de Oliveira, to appear in *Theor. Biosci.* **120** (2001).
- [36] A.L. Goodman, J.I. Kapusta and A.Z. Mekjian, *Phys. Rev.* **C30**, 851 (1984).
- [37] X. Campi, *J. Phys.* **A19**, L917 (1986); for percolation itself, see D. Stauffer and A. Aharony *Introduction to Percolation Theory*, Taylor and Francis, London (1994).
- [38] M.L. Gilkes et al, *Phys. Rev. Lett.* **73**, 1590 (1994); J.B. Elliot et al, *Phys. Rev.* **C55**, 1319 (1997).
- [39] J. Aichelin, *Phys. Rep.* **202**, 233 (1991).
- [40] A. Lejeune, J. Perdang and J. Richert, *Phys. Rev.* **E60**, 2601 (1999).

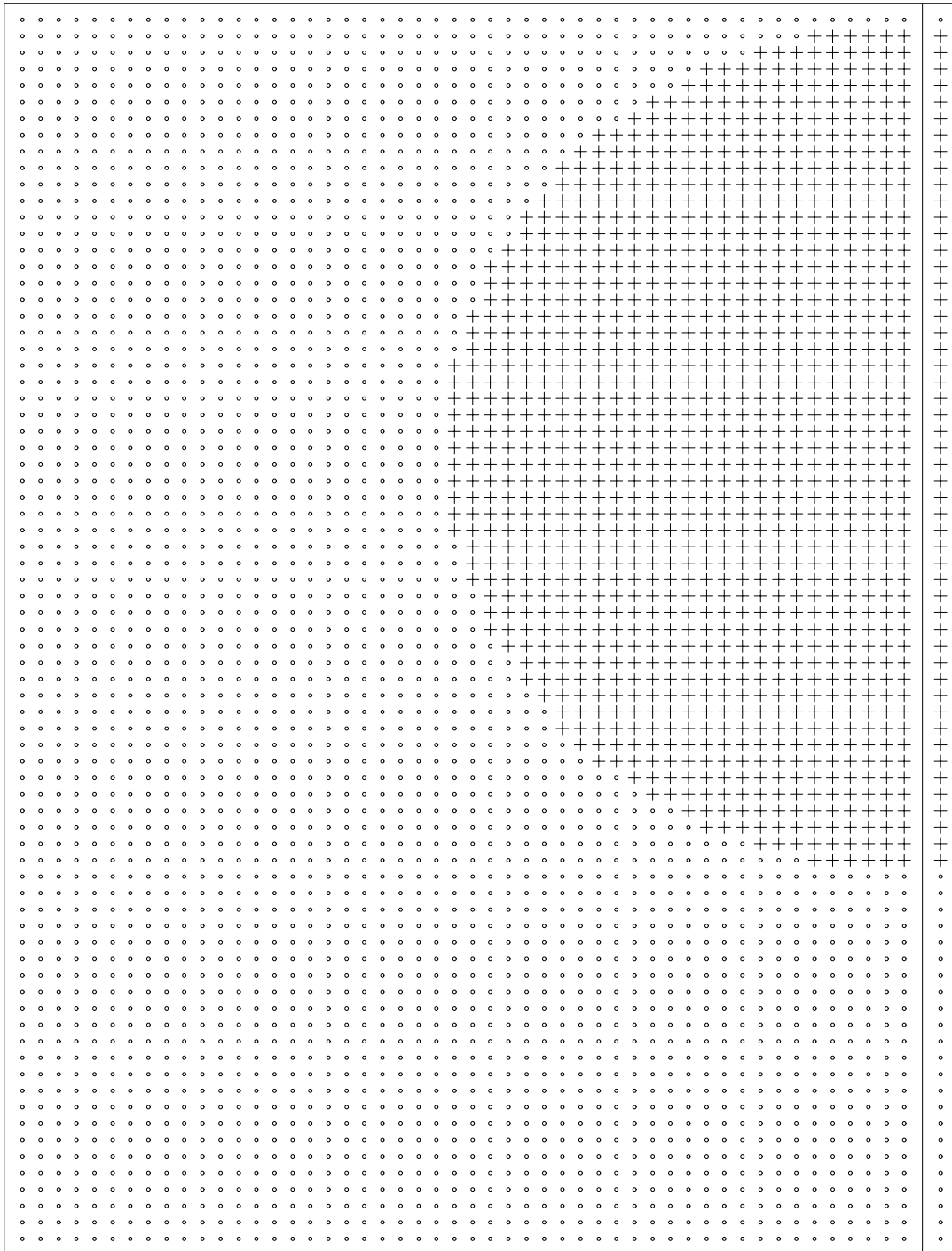
- [41] X. Campi and H. Krivine, *Nucl. Phys.* **A620**, 46 (1997); S.K. Samaddar and S. Das Gupta, *Phys. Rev.* **C61**, 034610 (2000).
- [42] R.J. Baxter, *Exactly Solved Models in Statistical Mechanics*, Academic Press (1989).
- [43] L. Beaulieu et al, *Phys. Rev. Lett.* **84**, 5971 (2000); S. Das Gupta, A. Majumder, S. Pratt and A. Mekjian, pre-print nucl-th/9903007.
- [44] O. Sotolongo-Costa, Y. Moreno-Vega, J.J. Lloveras-González and J.C. Antoranz, *Phys. Rev. Lett.* **76**, 42 (1996).
- [45] J. Unguris, R.J. Celotta, and D.T. Pierce, *Phys. Rev. Lett.* **67**, 140 (1991).
- [46] B. Heinrich and J.A.C. Bland, *Ultrathin Magnetic Structures* (Springer, Berlin, 1994), Vol. 2.
- [47] B. Dieny, *J. Magn. Magn. Mater.* **136**, 335 (1994).
- [48] L.F. Schelp, G. Tosin, M. Carara, M.N. Baibich, A.A. Gomes and J. E. Schmidt, *Appl. Phys. Lett.* **61**, 12 (1992); *J. Magn. Magn. Mater.* **121**, 399 (1993); G. Tosin, *MSc. Thesis*, Universidade Federal do Rio Grande do Sul, Porto Alegre, Brazil (1992).
- [49] K. Kawasaki, in *Phase Transitions and Critical Phenomena*, edited by C. Domb and M. S. Green, Academic, New York (1972), Vol. 2, p. 443, and references therein.
- [50] E.A.M. van Alphen, P.A.A. van der Heijden and W.J.M. de Jonge, *J. Magn. Magn. Mater.* **140-144**, 609 (1995).
- [51] K.G. Wilson, *Sci. Am.* **241**, 140 (August 1979).

Figure Captions

- I.1 Schematic representation of a water drop pending from a vertical wall. This is the initial condition adopted in [1]. After many boundary relaxations, the equilibrium geometrical aspect of the drop is measured, and the results [1] are in excellent agreement with real drops.
- II.1 Stages of one drop formation using the lattice drop model. The values of the parameters are $W = 40$, $N = 150$, $g = 0.1$ and $F = 20$. The numbers over the figures correspond to the time counted since the previous drop disconnection.
- II.2 Center of mass position *versus* time. We can see two regimes. One before the neck formation and another when the drop starts breaking. The usual oscillations in the center of mass position are not present since inertia is not considered in our model. The drop here is the same shown in the figure II.1.
- II.3 Area *versus* perimeter, for the same drop as figure II.1.
- II.4 Perimeter over area *versus* time, for the same drop again.
- II.5 First return maps of some time series obtained from the lattice drop model, for different values of flux. The other parameters are $g = 0.5$, $N = 150$, $W = 20$.
- II.6 Mean fluctuation of the same time series of figure II.5. For these and all other cases we tested, both experimental and simulated, the Hurst exponent is $\alpha = 0.00$.
- III.1 A $\log \times \log$ plot of the correlations between the moments of orders 3 and 2, with slope $\lambda_{3/2}$, and of orders 5 and 2, with slope $\lambda_{5/2}$, are shown, as obtained in simulations. Event-by-event analysis of experimental data exhibit the same strong correlations. The simulations were performed on a system composed of 216 nucleons on a cubic 3D lattice, and data was extracted from a total of 10,000 realisations. The initial temperature, corresponding to the excitation energy of the intermediate nucleus, was 8.50 in units of the Onsager critical temperature for the 2D Ising model. A Fermi-gas caloric curve was used, and the surface/bulk time ratio was $a = 0.998$. The slopes satisfy the consistency conditions and yield a value for the Fisher exponent $\tau = 2.18$, consistent with 3D percolation. It is worth mentioning that this value can also be obtained with a linear caloric curve, and appears to be somewhat insensible to the value of a as well.
- III.2 The $\log \times \log$ plot shows the matching of the slopes of the second moments of the fragment distributions, computed below and above the transition, in a procedure described in the text. Data was acquired from the same runs that were used for figure III.1. The resulting value for γ is consistent with the 3D percolation universality class.
- IV.1 Experimental size probability distribution of the fragments produced by a mercury

- drop falling onto the floor.
- IV.2 Simulated size probability distribution of fragments, according to our dynamic lattice model. The mercury drop is represented by a cluster of black pixels (spin *up*) on a square lattice, initially with 321 pixels. The energy is $E = 1800$, $r = 50$ and $k = 0.2$ (see text). The plot corresponds to 5000 independent falls.
- IV.3 The same as the previous, for a cubic lattice where the initial drop occupies 179 pixels. $E = 179$, $r = 50$ and $k = 0.9$.
- V.1 Initial magnetic grain with two domains of Ising spins, no external applied field.
- V.2 Snapshot of the same grain, after gradually increasing the applied field h . The resulting magnetisation m is also shown.
- V.3 Another snapshot. The magnetic domain wall is bent, but not yet sliding against the grain boundaries.
- V.4 Domain wall starts to slide.
- V.5 Due to sliding, the magnetisation increases now very fast.
- V.6 Saturated magnetic grain.
- V.7 Complete hysteresis curve. It starts from the virgin grain (figure V.1), following branch 0 as the external field gradually increases. After saturation, the field is gradually decreased and then inverted, the system following branch 1. Branch 2 corresponds to the reverse path, relative to 1.
- VI.1 Schematic representation of a stripe of material A sandwiched by B atoms. We consider a square lattice and first-neighbour interactions.
- VI.2 Mean roughness variation as a function of annealing temperature T_a for different values of $W = 6$ (circles), 8 (squares), 10 (diamonds), 12 (triangles), and 15 (crosses). Averages were calculated with $N = 100$ different samples, and typical error bars are shown. Lines are cubic splines used as guides to the eyes. The insets show snapshots of the final $W = 6$ interface configuration at T_0 , for some values of T_a . For $T_a = 2.52$ the A layer breaks into clusters.

FIGURE I.1 – de Oliveira et. al.



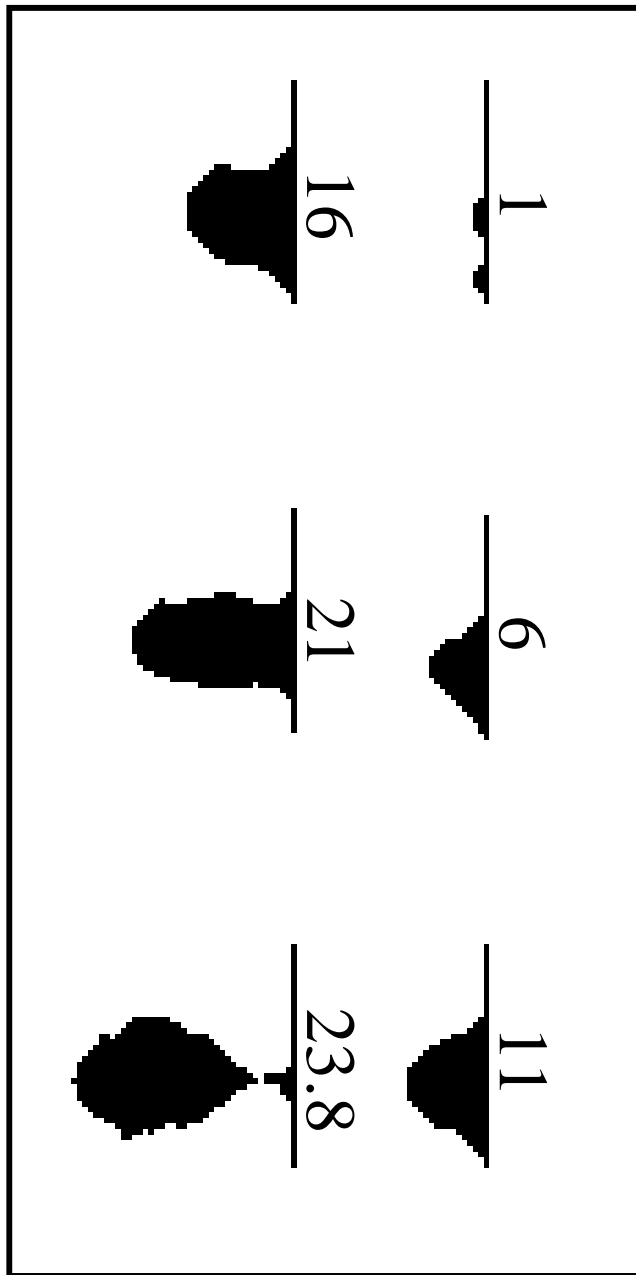


FIGURE II.1 - de Oliveira et. al.

FIGURE III.1 – de Oliveira et. al.

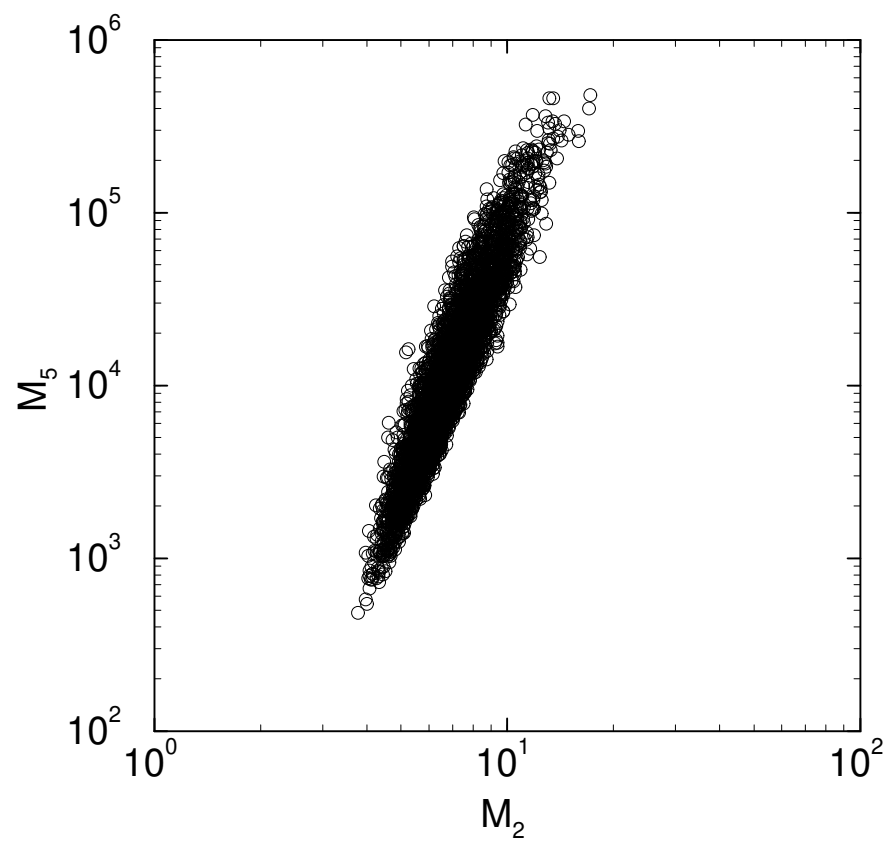
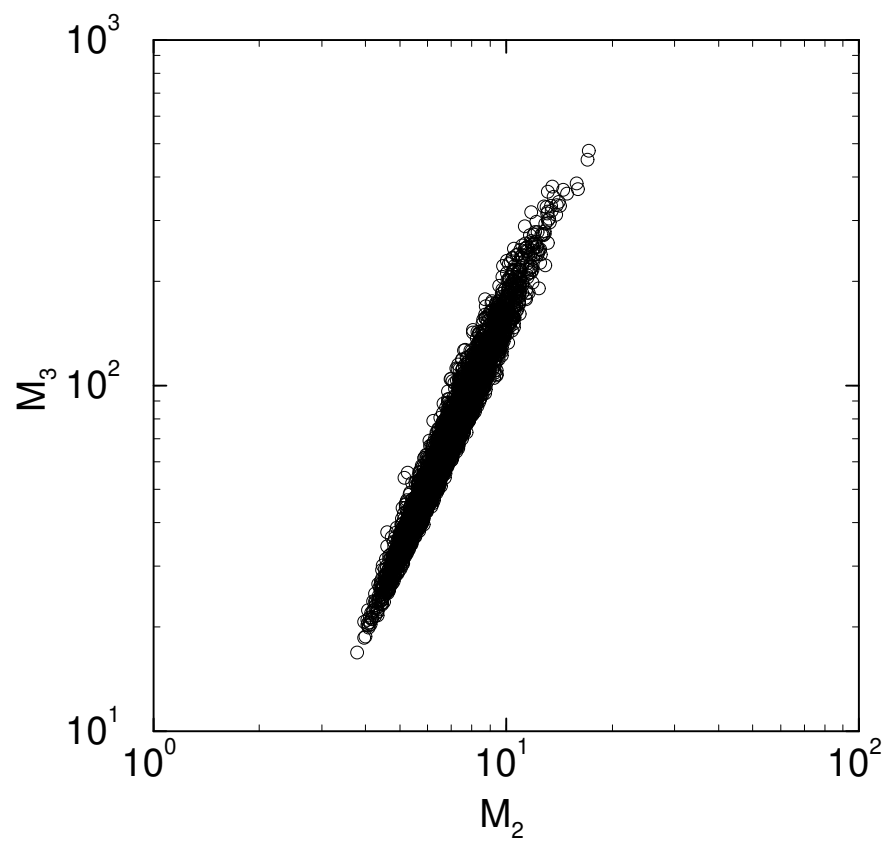
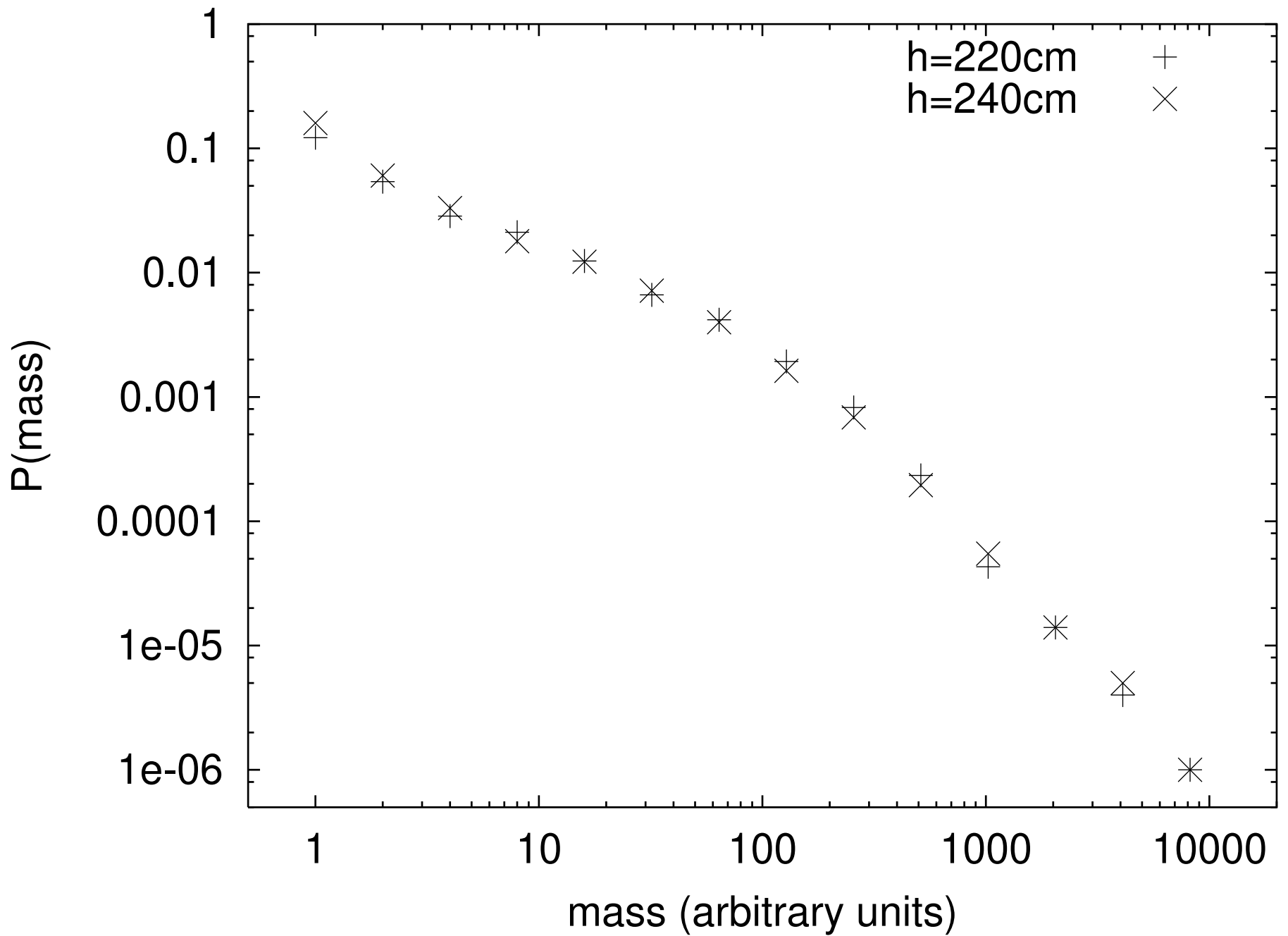


FIGURE IV.1 - de Oliveira et. al.



$h = 0.000$ $m = 0.000$

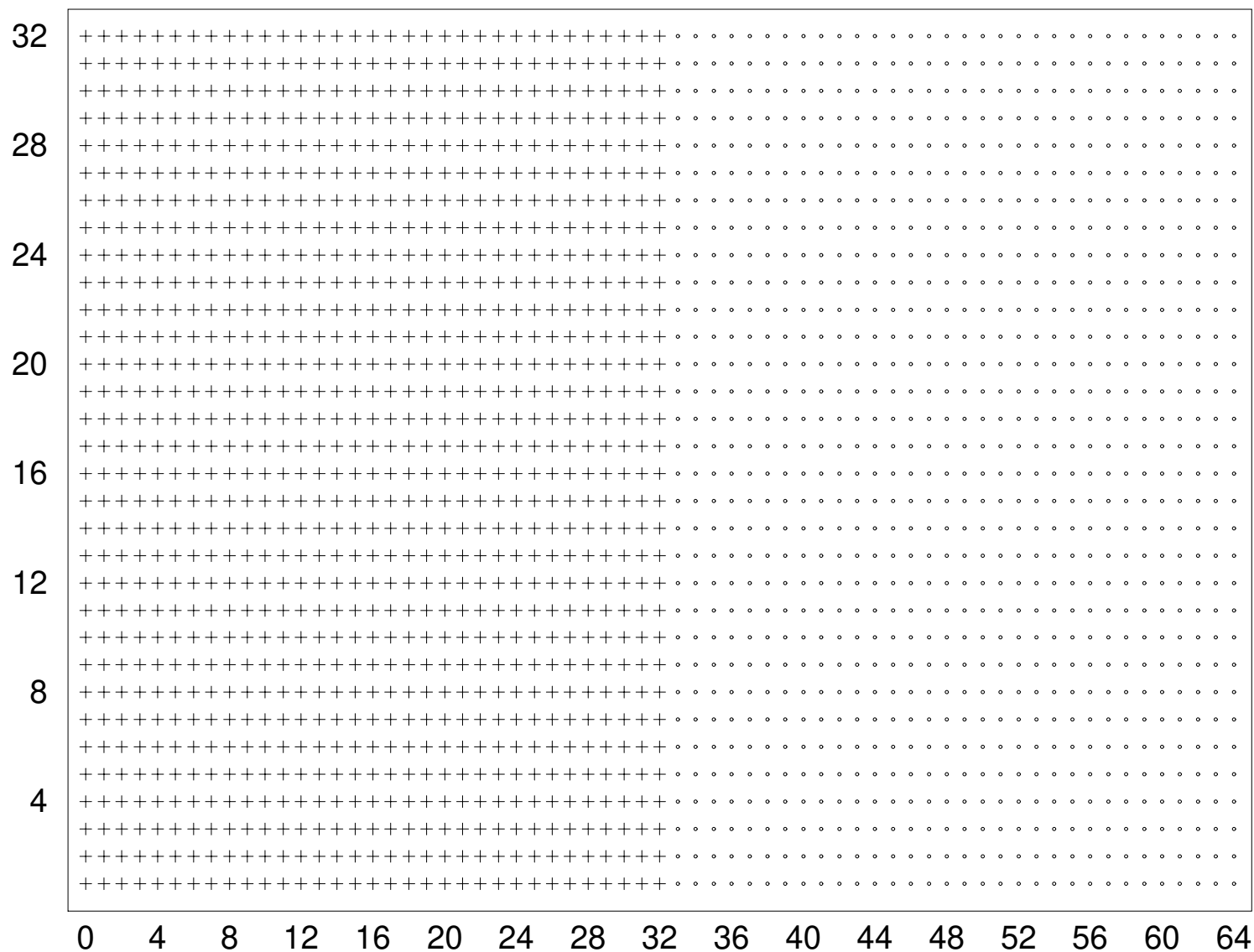


FIGURE V.1 – de Oliveira et. al.

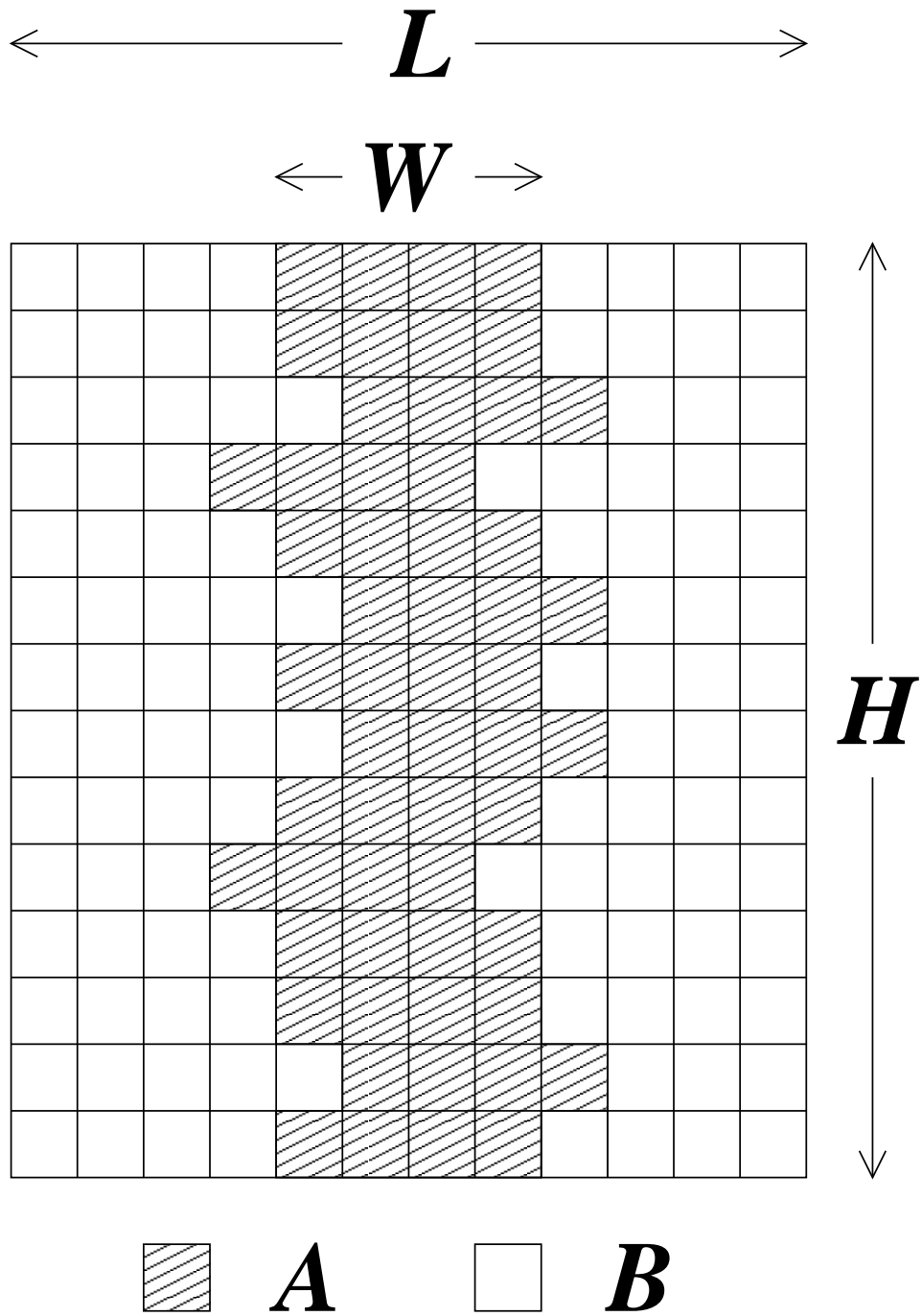


FIGURE VI.1 - de Oliveira et. al.

FIGURE II.2 - de Oliveira et. al.

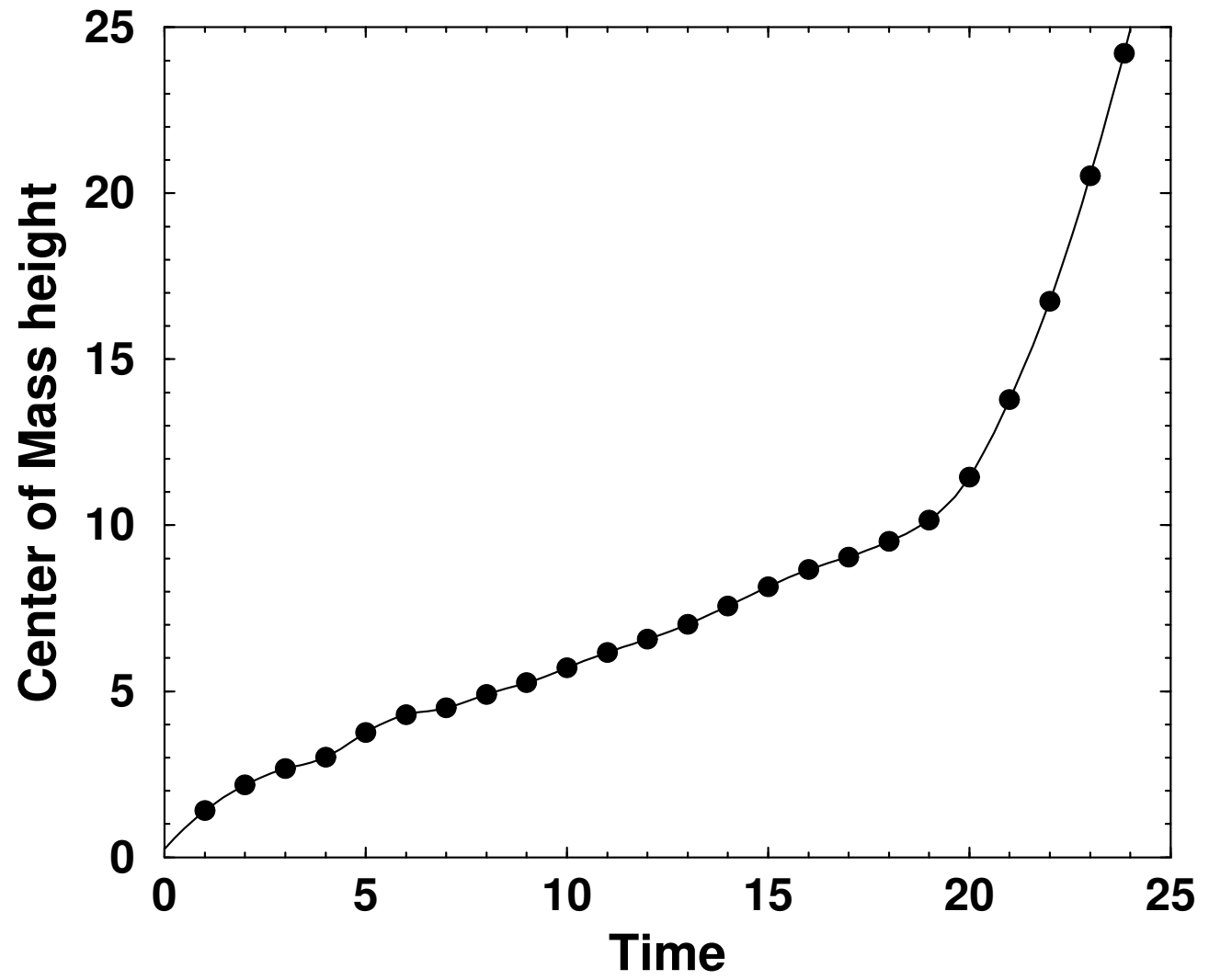


FIGURE III.2 – de Oliveira et. al.

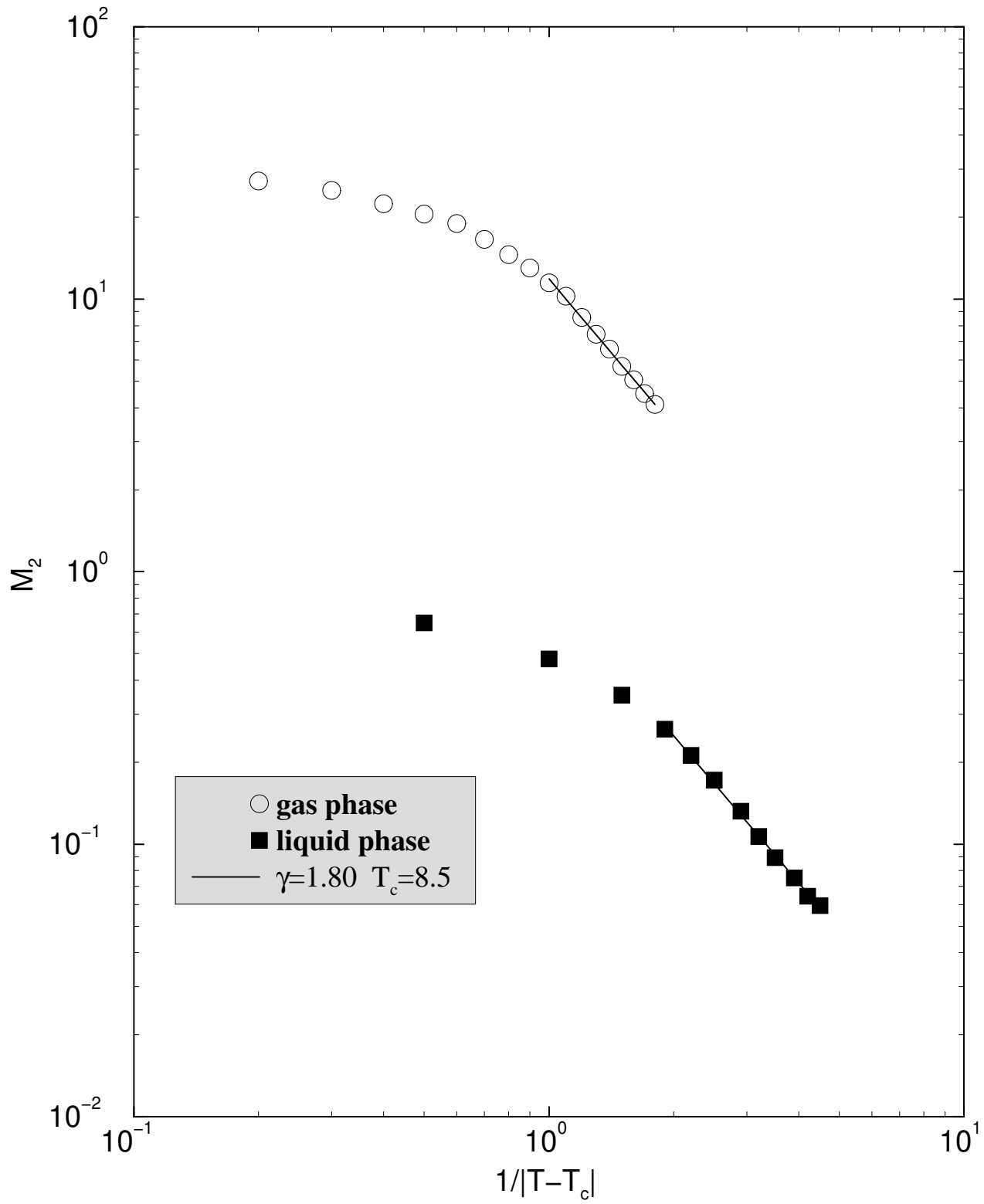
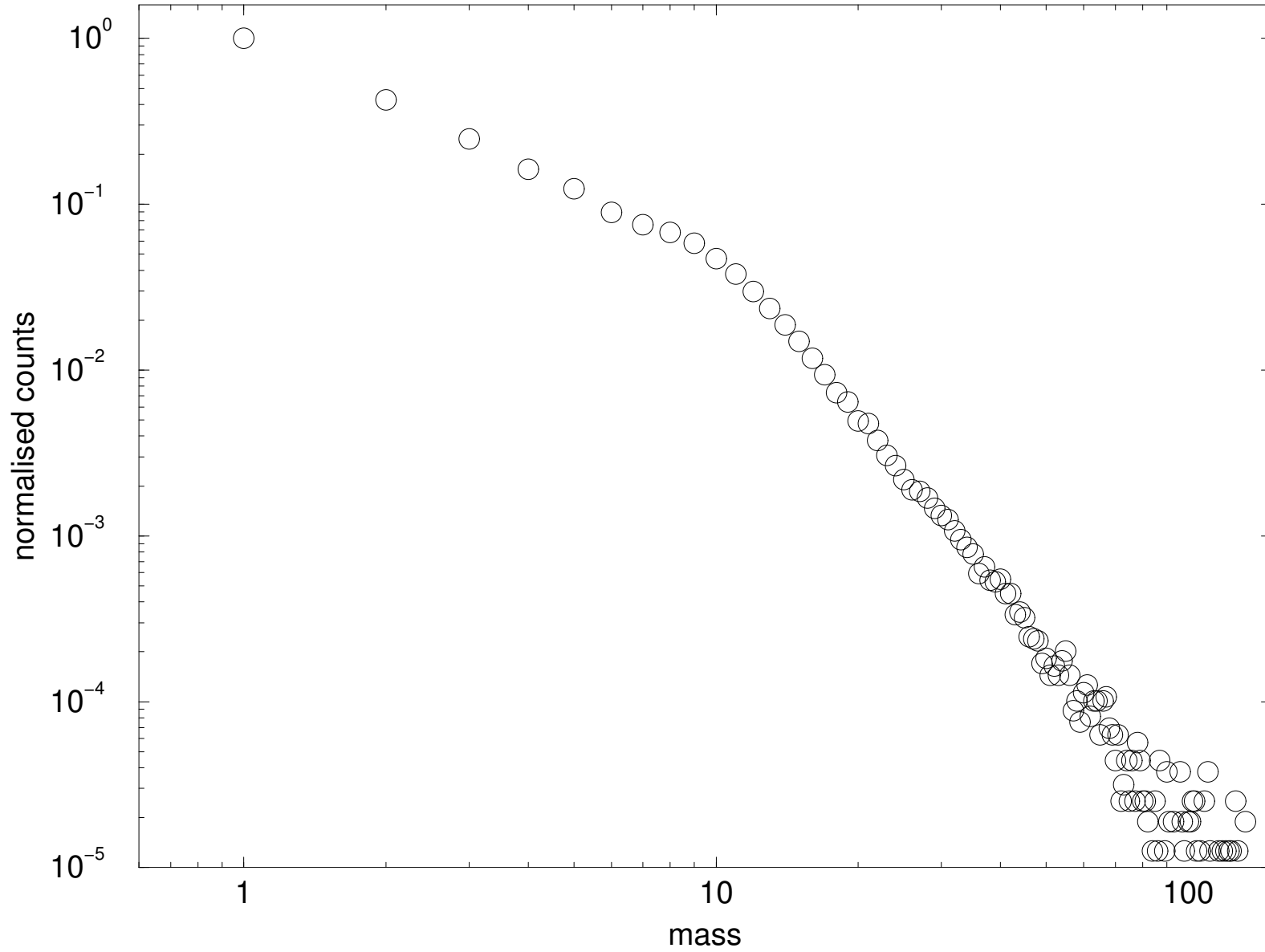


FIGURE IV.2 – de Oliveira et. al.

fragment distribution

square lattice



$h = 0.300$ $m = 0.049$

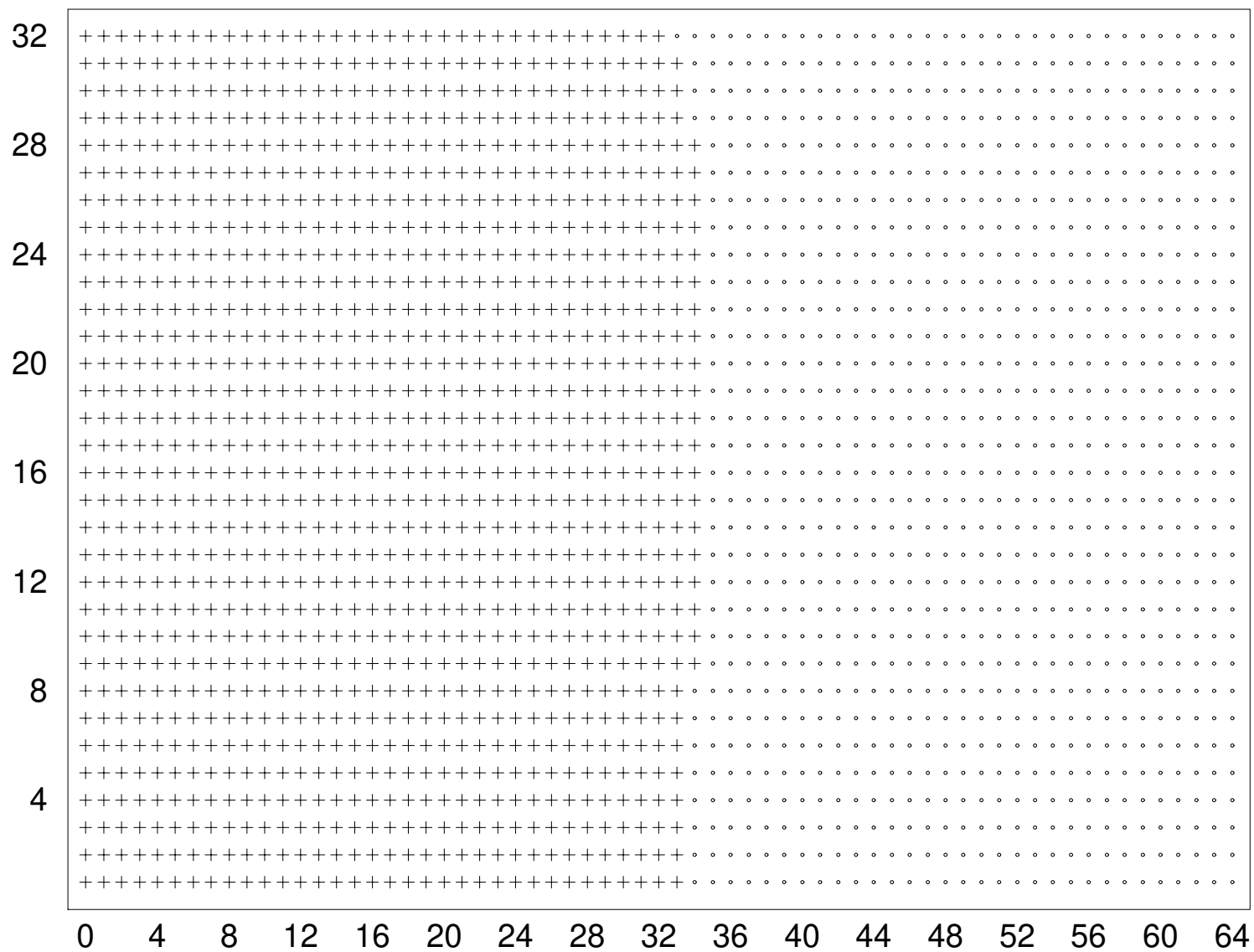


FIGURE V.2 – de Oliveira et. al.

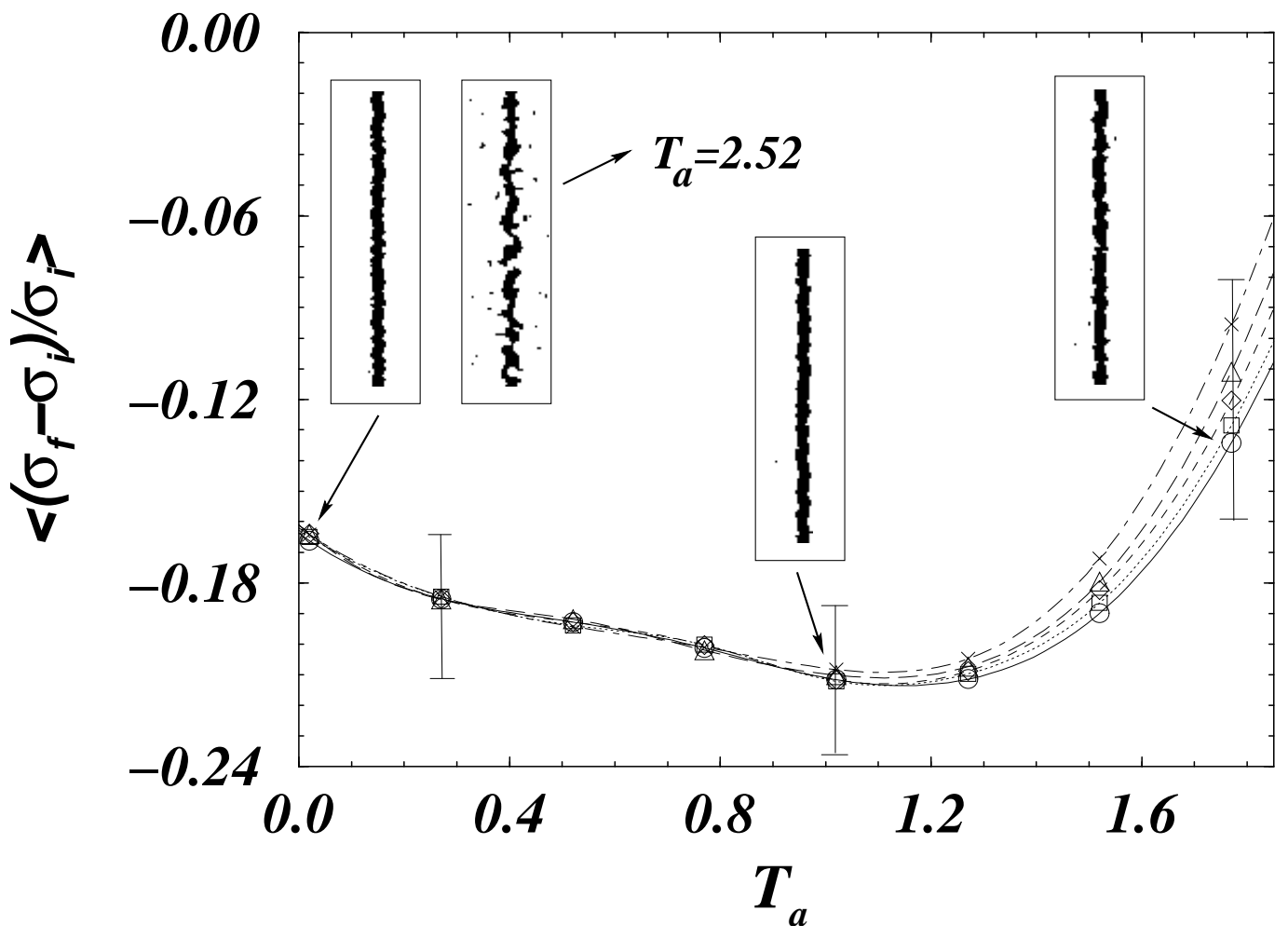


FIGURE VI.2 - de Oliveira et. al.

FIGURE II.3 - de Oliveira et. al.

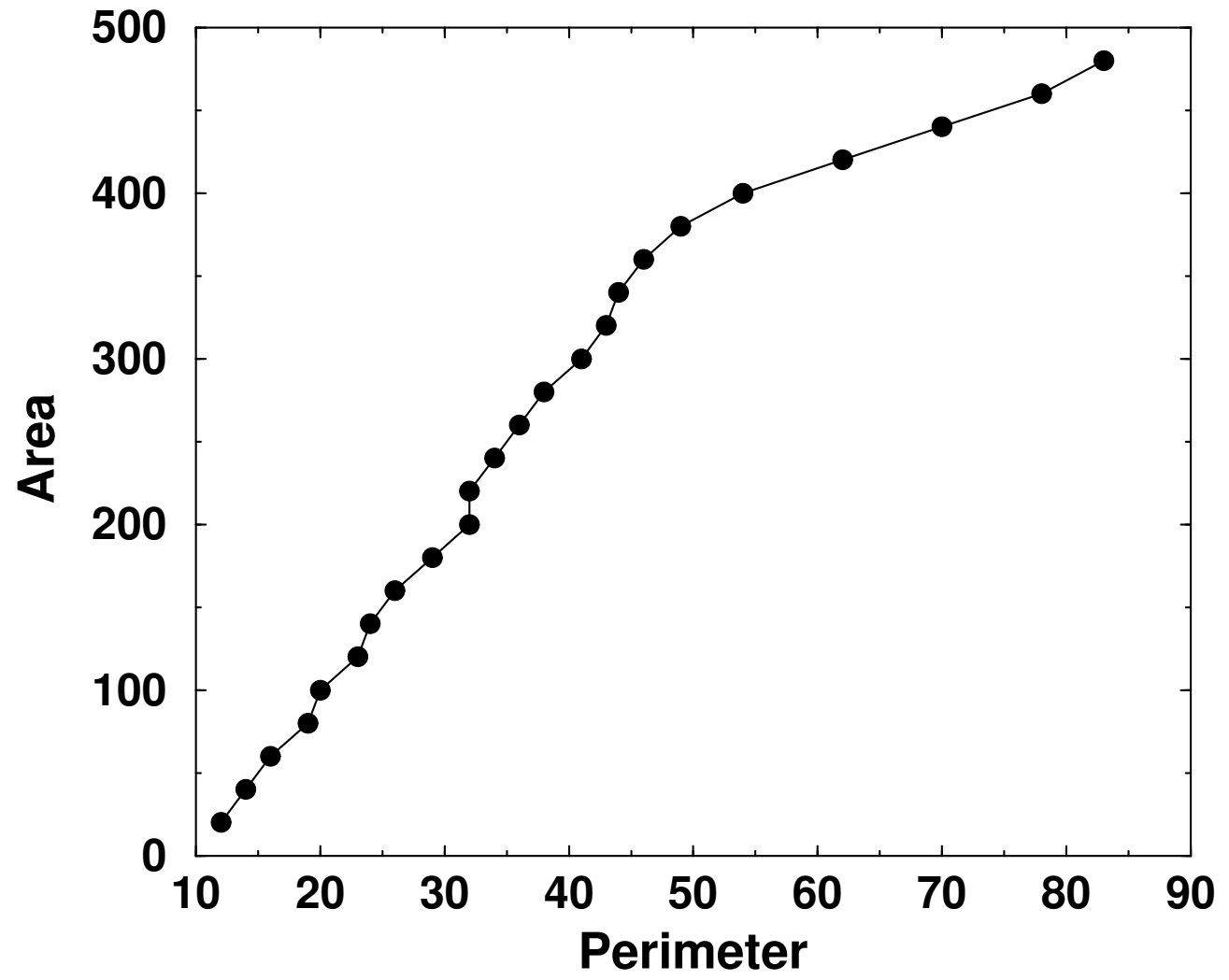
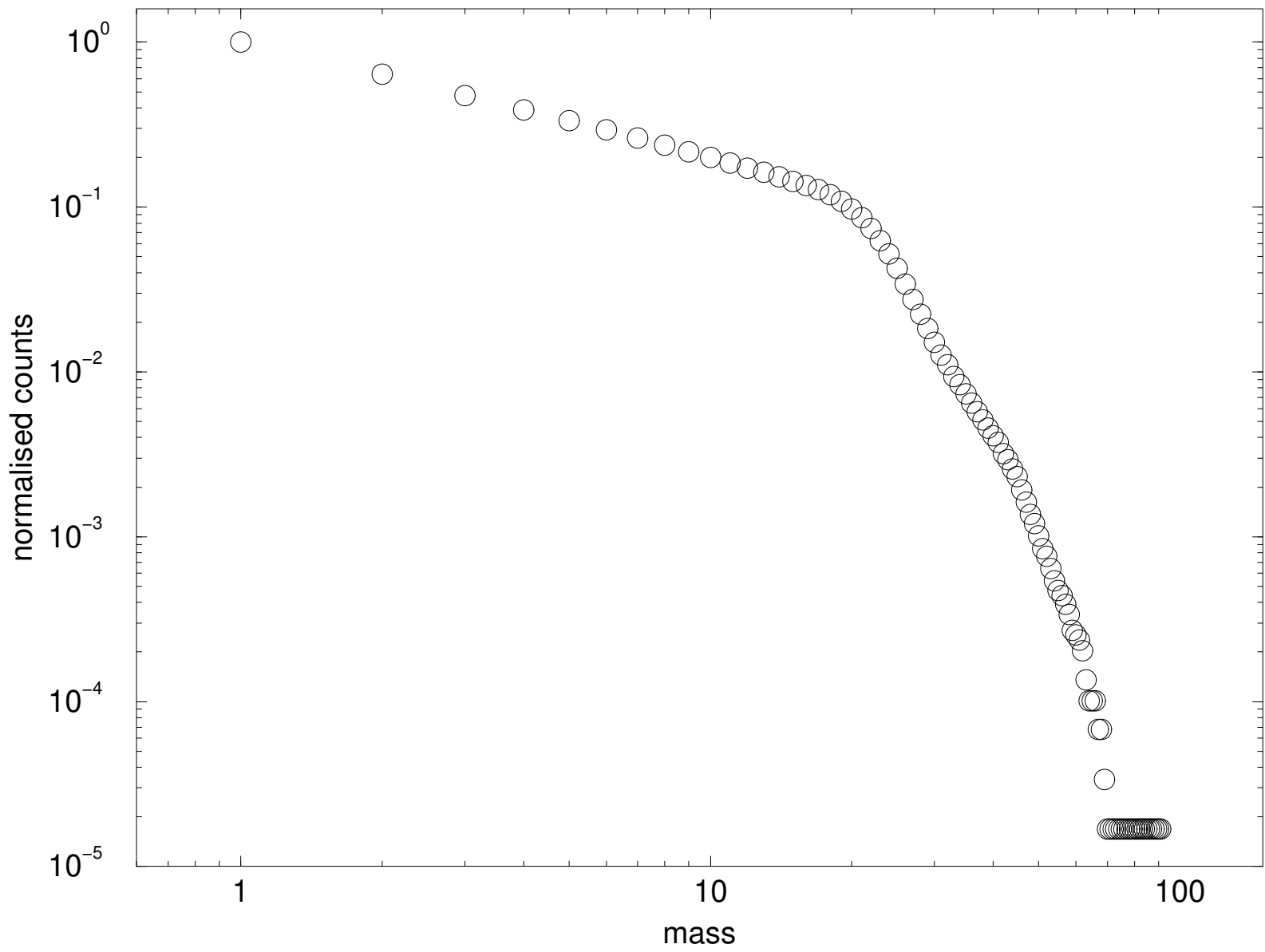


FIGURE IV.3 – de Oliveira et. al.
fragment distribution

cubid lattice



$h = 0.600$ $m = 0.136$

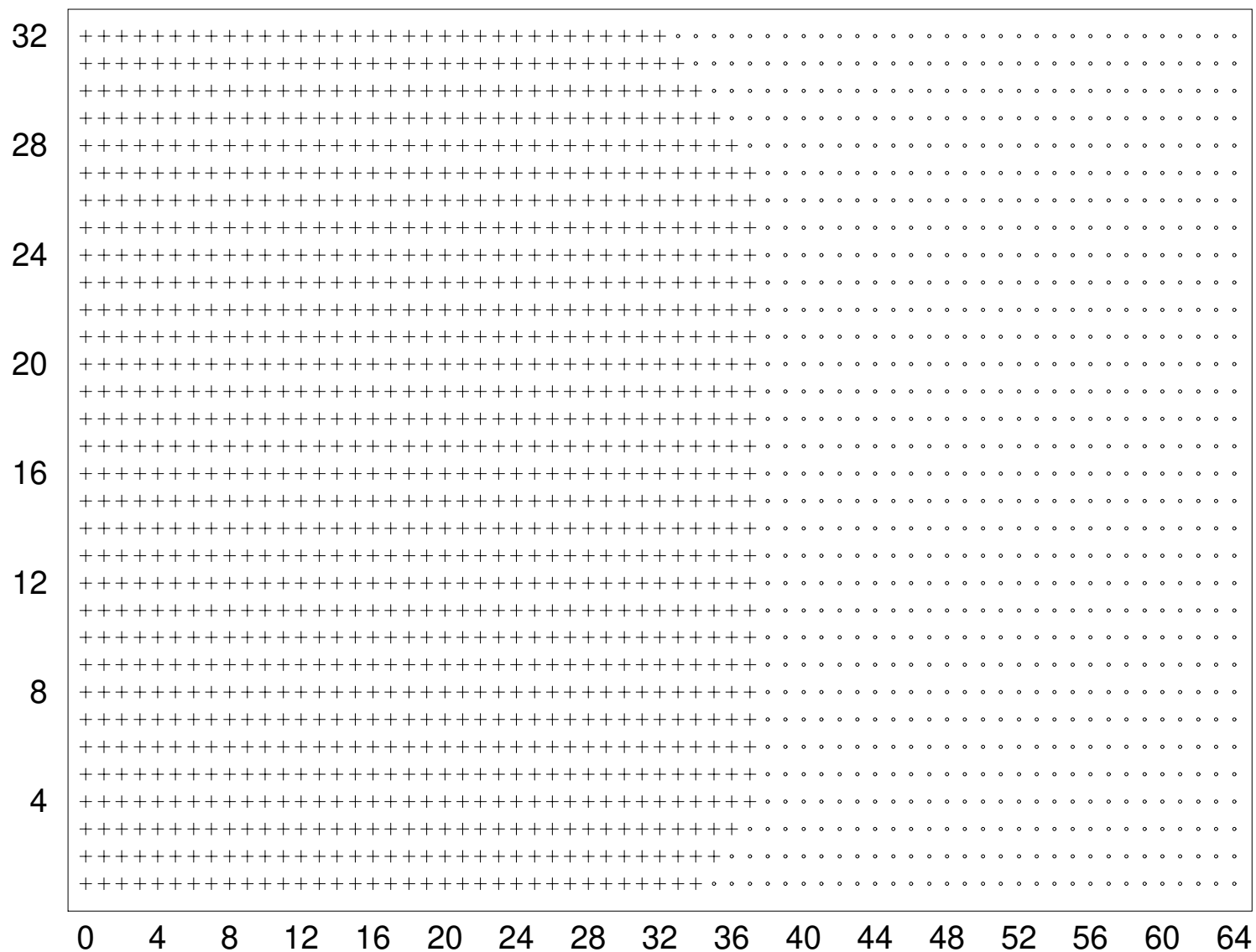
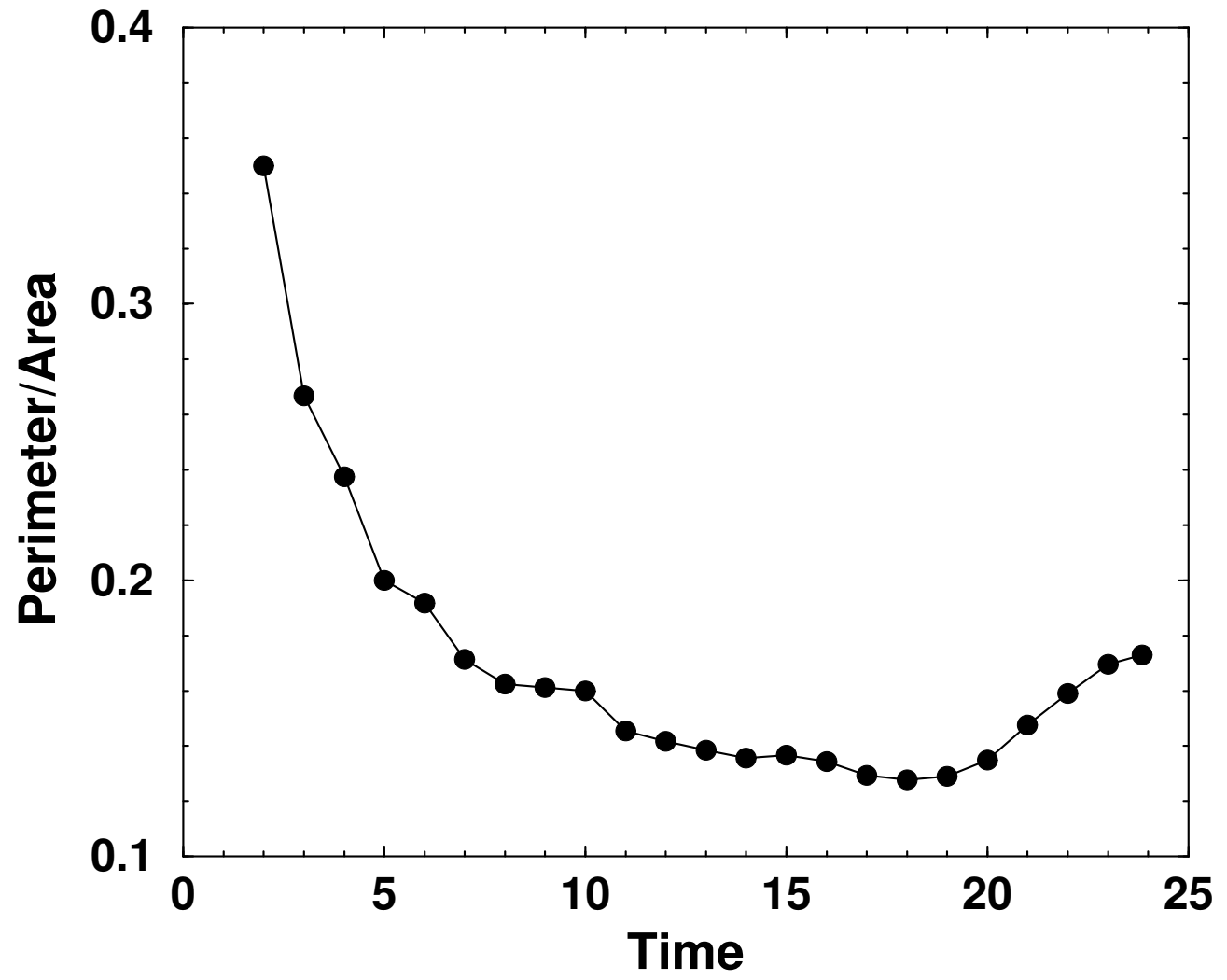


FIGURE V.3 – de Oliveira et. al.

FIGURE II.4 - de Oliveira et. al.



$h = 0.900$ $m = 0.291$

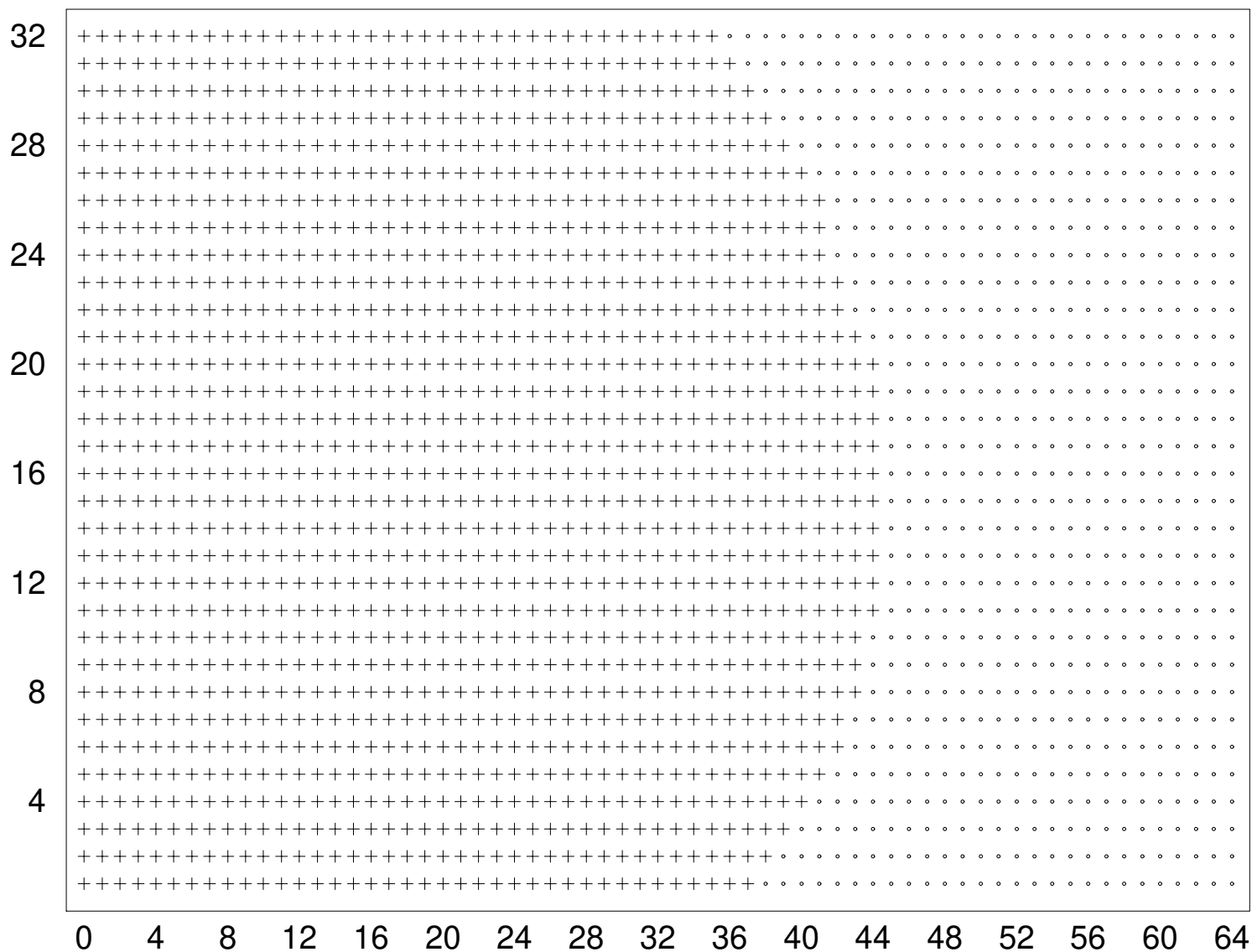


FIGURE V.4 – de Oliveira et. al.

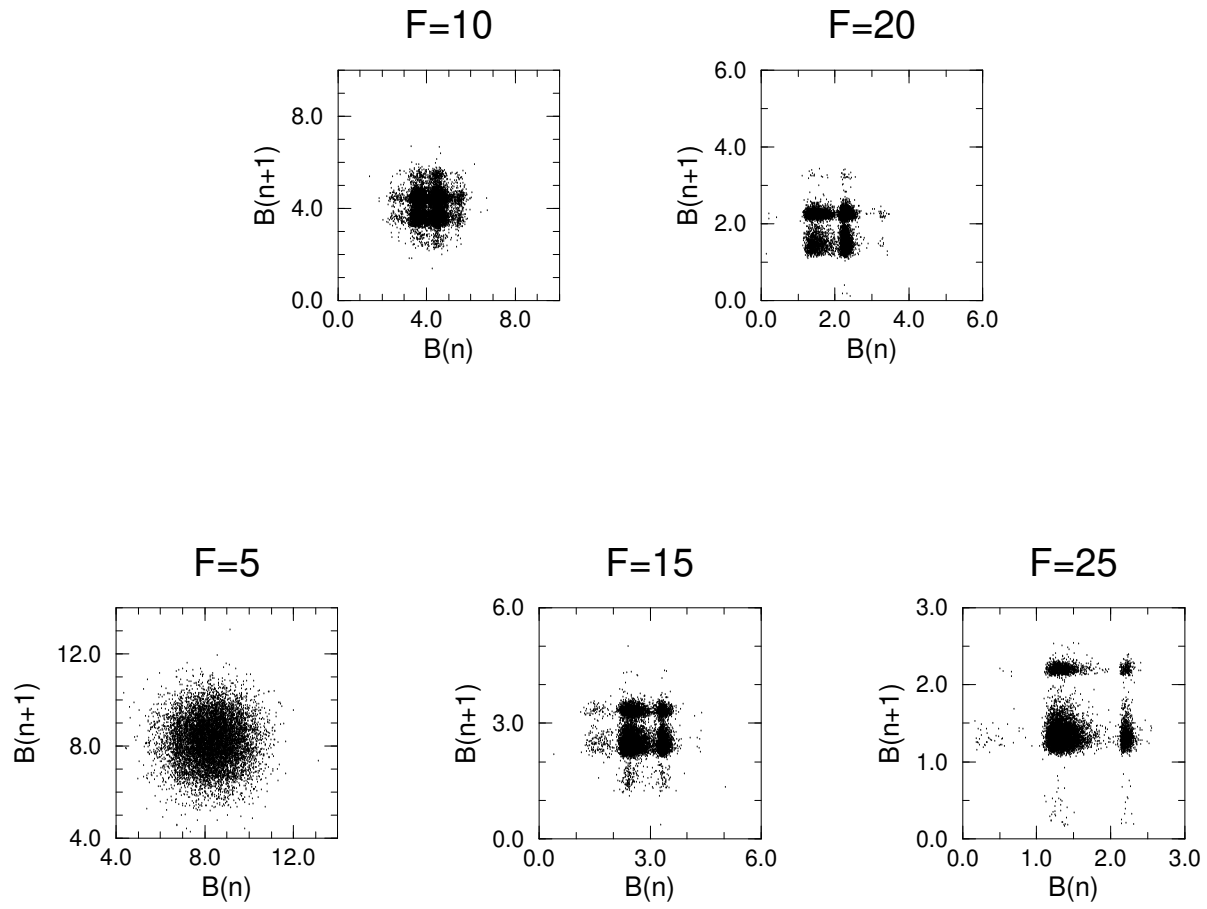


FIGURE II.5 – de Oliveira et. al.

$h = 1.200$ $m = 0.595$

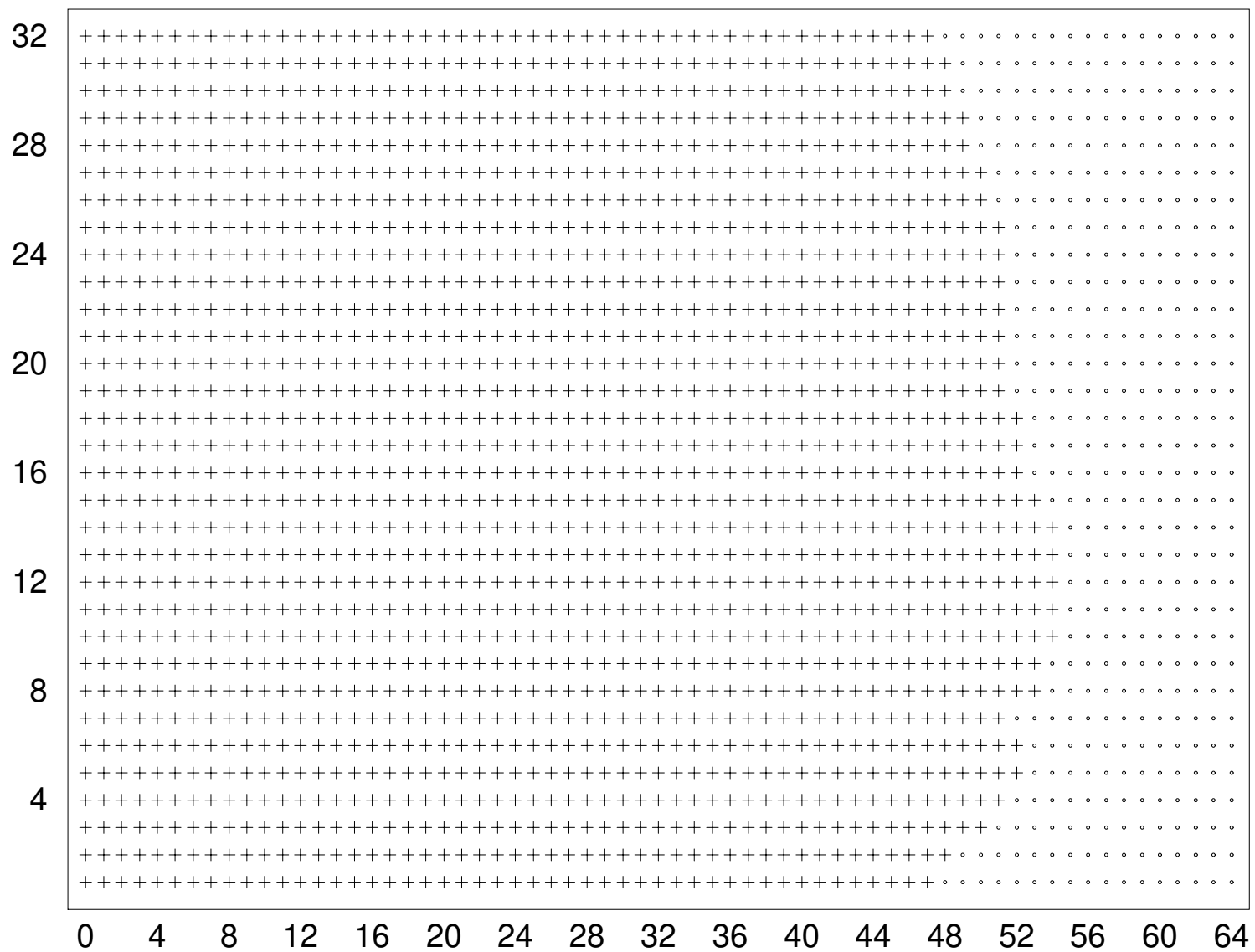


FIGURE V.5 – de Oliveira et. al.

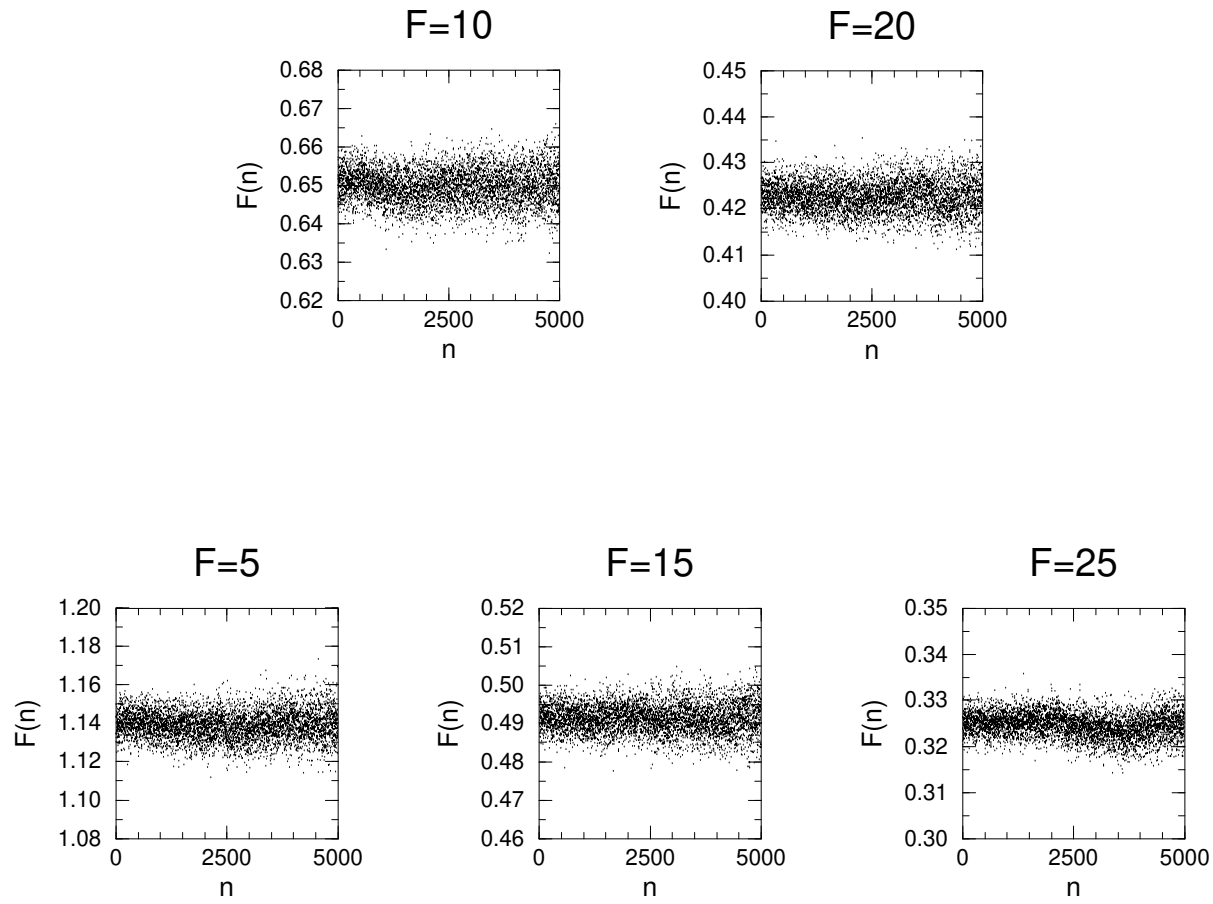


FIGURE II.6 – de Oliveira et. al.

$h = 1.500$ $m = 1.000$

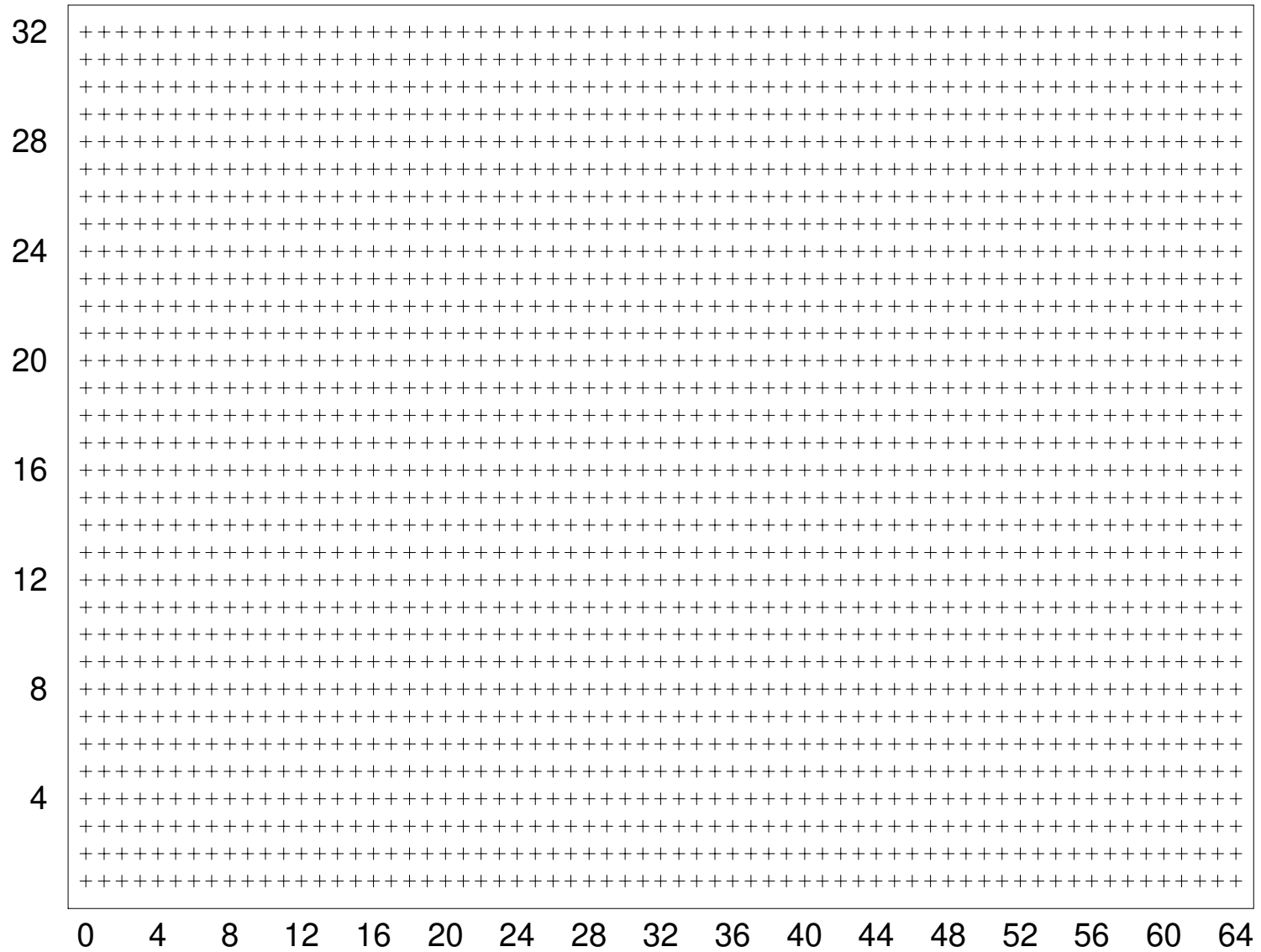


FIGURE V.6 – de Oliveira et. al.

FIGURE V.7 – de Oliveira et. al.

